



The Impact of Deorbiting Space Debris on Stratospheric Ozone

Prepared for:

Environmental Management Division
Space and Missile Systems Center
El Segundo, California

Prepared by:

TRW Space and Electronics Group

Peter D. Lohn, Ph.D.
Eric Y. Wong, Ph.D.

in coordination with:

Mario J. Molina, Ph.D.
Professor, Department of Earth and Planetary Sciences
Massachusetts Institute of Technology

and

M. Richard Denison
Denison Development Inc.

31 May 1994

Report Documentation Page

Report Date 31051994	Report Type N/A	Dates Covered (from... to) -
Title and Subtitle The Impact of Deorbiting Space Debris on Stratospheric Ozone		Contract Number
		Grant Number
		Program Element Number
Author(s) Lohn, Peter D., Wong, Eric Y.,		Project Number
		Task Number
		Work Unit Number
Performing Organization Name(s) and Address(es) TRW and Electronics Group One Space Park, Redondo Beach, CA 90278		Performing Organization Report Number
Sponsoring/Monitoring Agency Name(s) and Address(es)		Sponsor/Monitor's Acronym(s)
		Sponsor/Monitor's Report Number(s)
Distribution/Availability Statement Approved for public release, distribution unlimited		
Supplementary Notes		
Abstract		
Subject Terms		
Report Classification unclassified		Classification of this page unclassified
Classification of Abstract unclassified		Limitation of Abstract UU
Number of Pages 86		



The Impact of Deorbiting Space Debris on Stratospheric Ozone

Prepared for:

Environmental Management Division
Space and Missile Systems Center
El Segundo, California

Prepared by:

TRW Space and Electronics Group

Peter D. Lohn, Ph.D.
Eric Y. Wong, Ph.D.

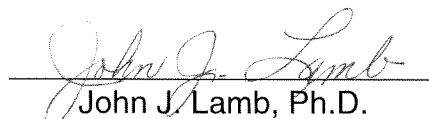
in coordination with:

Mario J. Molina, Ph.D.
Professor, Department of Earth and Planetary Sciences
Massachusetts Institute of Technology

and

M. Richard Denison
Denison Development Inc.

Approved by:


John J. Lamb, Ph.D.
Program Manager

31 May 1994

THE IMPACT OF DEORBETING SPACE DEBRIS ON STRATOSPHERIC OZONE

CONTENTS

1. Introduction
2. Orbital Debris Population & Flux to the Stratosphere
3. Reentry Mechanics and Heating of Deorbiting Debris
4. Depletion of Stratospheric Ozone by Heterogeneous Mechanisms
5. Depletion of Stratospheric Ozone by Homogeneous Mechanisms
6. Summary and Conclusions

1. Introduction and Summary

The Environmental Management of the Space & Missile Systems Command has set out to evaluate the depletion of stratospheric ozone caused by Air Force activities in space. Potential destruction of ozone by launch vehicle exhaust is one item of concern (Ref. 1.1). The use of advanced propellants to minimize launch-induced ozone destruction is discussed in a companion report. The present report describes a quantitative assessment of another potential destroyer of stratospheric ozone: deorbiting space debris.

The results of the present study lead to the conclusion that deorbiting space debris has very little impact on stratospheric ozone. The task-by-task analysis leading to this conclusion is summarized as follows:

Characterize the debris flux into the stratosphere.

Debris object density was characterized by size and altitude. Orbital decay was calculated and the results led to an estimate of the flux into the stratosphere as a function of object size. The results showed a preferential population of the stratosphere by smaller debris objects. The calculated stratospheric object density for one micrometer size particles is in reasonable agreement with measured values.

Calculate reentry trajectory and heating.

Several object sizes and materials were considered. In general, sub-millimeter size objects settle slowly through the stratosphere. Intermediate size objects (millimeter to decimeter) may melt/vaporize in or above the stratosphere. Larger objects (decimeters) may survive to the earth's surface. It is essential to account for the balance between convective heating and radiation heat loss to characterize the thermal response of the deorbiting debris. The trajectory/heating results provided initial conditions for assessment of ozone depletion by several mechanisms.

Evaluate ozone depletion by heterogeneous mechanisms.

Deorbiting debris provides several sources for deposition of small particles into the stratosphere. Two mechanisms, for example, are: direct orbital decay of small particles and stripping small particles from surfaces of larger space objects by aerodynamic drag forces generated during the deorbit/reentry process. The small particles provide active sites for heterogeneous reactions similar to those of the polar stratospheric cloud (PSC) particles. MIT performed experiments to measure the rate parameter for heterogeneous reactions in terms of the reaction probability. The measured data was used for the assessment of local and global effects on stratospheric ozone due to surface reactions. The impact on local ozone is evaluated based on a simple one-dimensional diffusion model for a single particle. Attention is focused on micrometer size particles because they provide the greatest total surface area. The resultant ozone depletion by heterogeneous mechanisms is estimated to be small: 10^4 - 10^5 years to destroy one percent of the stratospheric ozone.

Evaluate ozone depletion by homogeneous mechanisms.

Deorbiting debris reentering the stratosphere at hypersonic speeds creates a high temperature region between the bow shock and the body. The temperature immediately behind the shock reaches temperatures as high as 20,000 degrees Kelvin. At such extreme temperature large amounts of nitric oxide will be produced according to the Zeldovich mechanism and ambient ozone is subsequently consumed through the nitric oxide catalytic cycle. An additional source of nitric oxide is generated as pyrolysis products from spacecraft paint or ablation materials (material bound nitrogen). The impact of these mechanisms on stratospheric ozone is estimated to be small: destruction of one stratospheric ozone molecule per one billion per day by the material-bound nitrogen mechanism and one part per ten billion per year by the thermal mechanism.

2. Orbital Debris Population & Flux into the Stratosphere

The debris environment is characterized by specifying object density as a function of altitude and size. A large body of experimental data has been used to evaluate the object density and it is an ongoing activity for several groups (e.g., U. S. Air Force, NASA) to continually upgrade the debris characteristics.

Data sources for the debris environment include:

- 1) U. S. Space Command radar data for objects of size greater than ten centimeters,
- 2) Impact data from objects retrieved from space (e.g., LDEF, Solar Max) for smaller objects. This requires estimation of debris characteristics from crater/impact features,
- 3) Additional radar data for objects in the one to ten centimeter range.
- 4) Estimates of booster/satellite breakup characteristics.

Present estimates (Reference 2.1) show the population at 7000 to 8000 objects of size 10 cm or larger, 35,000 to 150,000 objects in the 1-10 cm range and 3-40 million under 1 cm. The altitude dependence of the object density is shown in Figure 2.1 (Reference 2.2) with the assumption of 35,000 objects of size greater than 1 cm. This population density can be scaled as the object density is updated. The flux of objects experienced by a spacecraft is the number density multiplied by a relative velocity (typically chosen as 10 km/s for LEO). The peak in object density at 800-1000 km is partly caused by booster breakup during launch of sun synchronous satellites while the peak at 1500 km is caused by breakup of NOAA satellite boosters as well as by USSR communication satellite activity.

Radar tracks 7000 objects. $D > 10$ cm
35000 objects with diameter > 1 cm

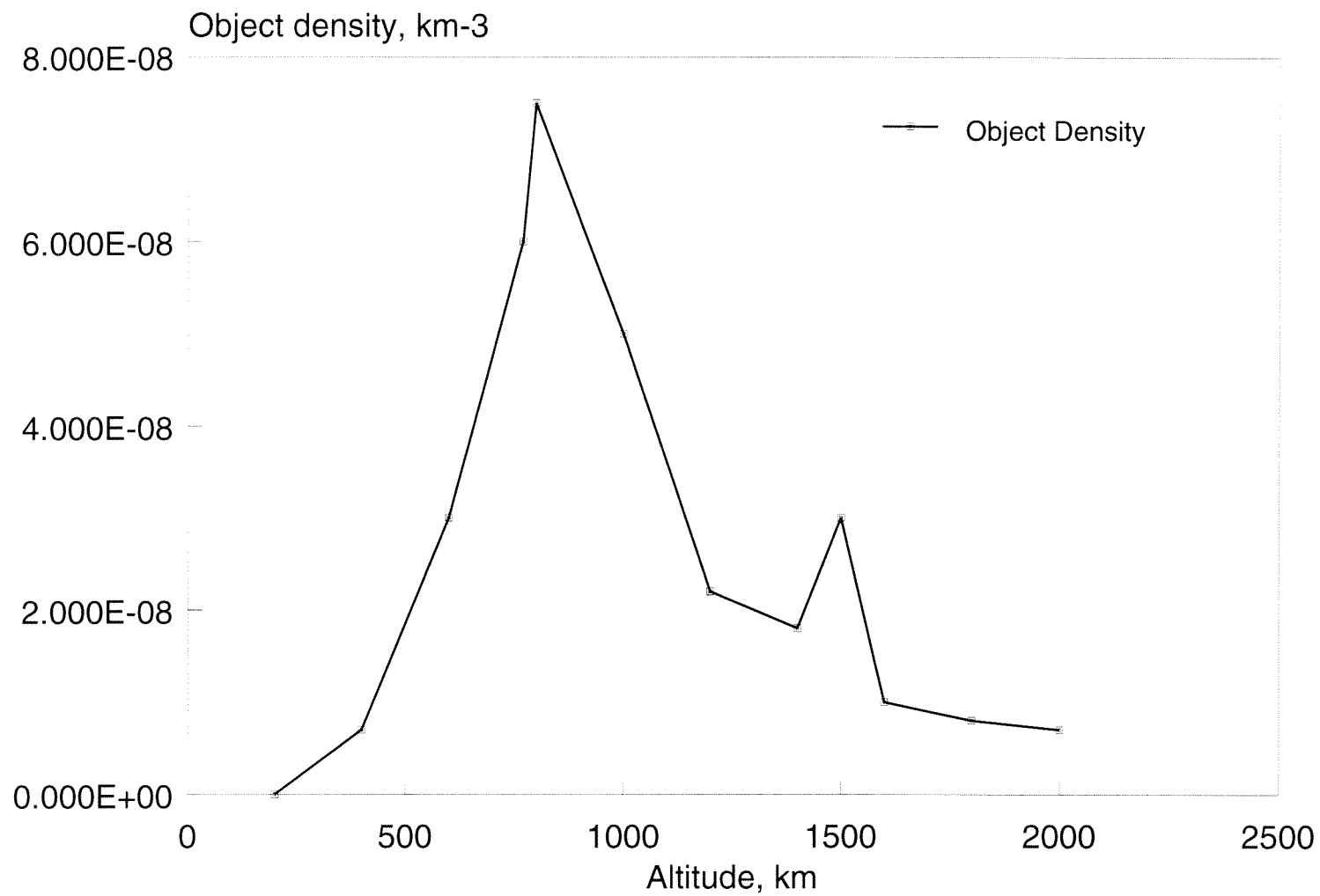


Figure 2.1. Orbital Debris Population

The orbital debris size distribution is a subject of continuing study. The size distribution used for this study is shown in Figure 2.2 and is taken from Reference 2.3. The ordinate of Figure 2.2 gives the number of particles of size greater than diameter d . The distribution is plotted from an analytical expression that gives approximately 7000 objects of size 10 cm or greater. While the figure shows the population increasing several orders of magnitude for the smaller size objects the object density may be overpredicted for object size less than 0.001 cm or 0.01 cm (Reference 2.4).

The debris population is increasing as a result of newly launched objects, explosions, collisions, and breakup of boosters and spacecraft. An estimate of the yearly growth of the debris population is given in Reference 2.3:

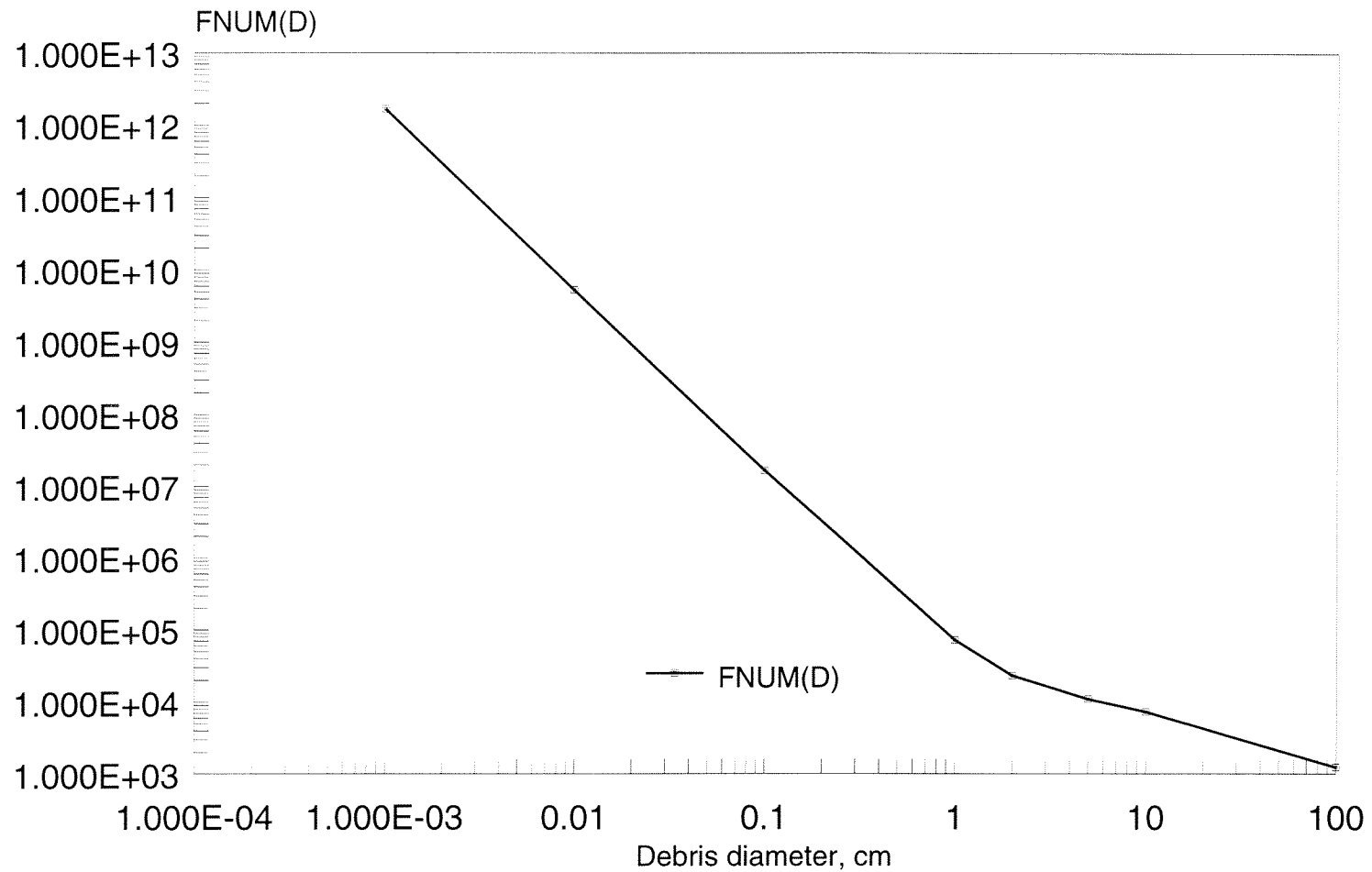
- o five percent for intact objects
- o two percent for fragments (increasing to four percent after the year 2010).

The debris object density and the subsequent flux into the stratosphere should be increased at these rates for later years.

FLUX INTO THE STRATOSPHERE

The process of orbital decay involves all the forces experienced by an object in space. The final decay process (altitudes below several hundred kilometers) is dominated by aerodynamic drag caused by the earth's atmosphere. A complete characterization of the decay process must include a balance of production terms (caused by new launches and

Low Earth Orbit (LEO), < 2000 km



$FNUM(D)$ =number of debris objects of diameter greater than D (cm)

Figure 2.2. Debris Size Distribution

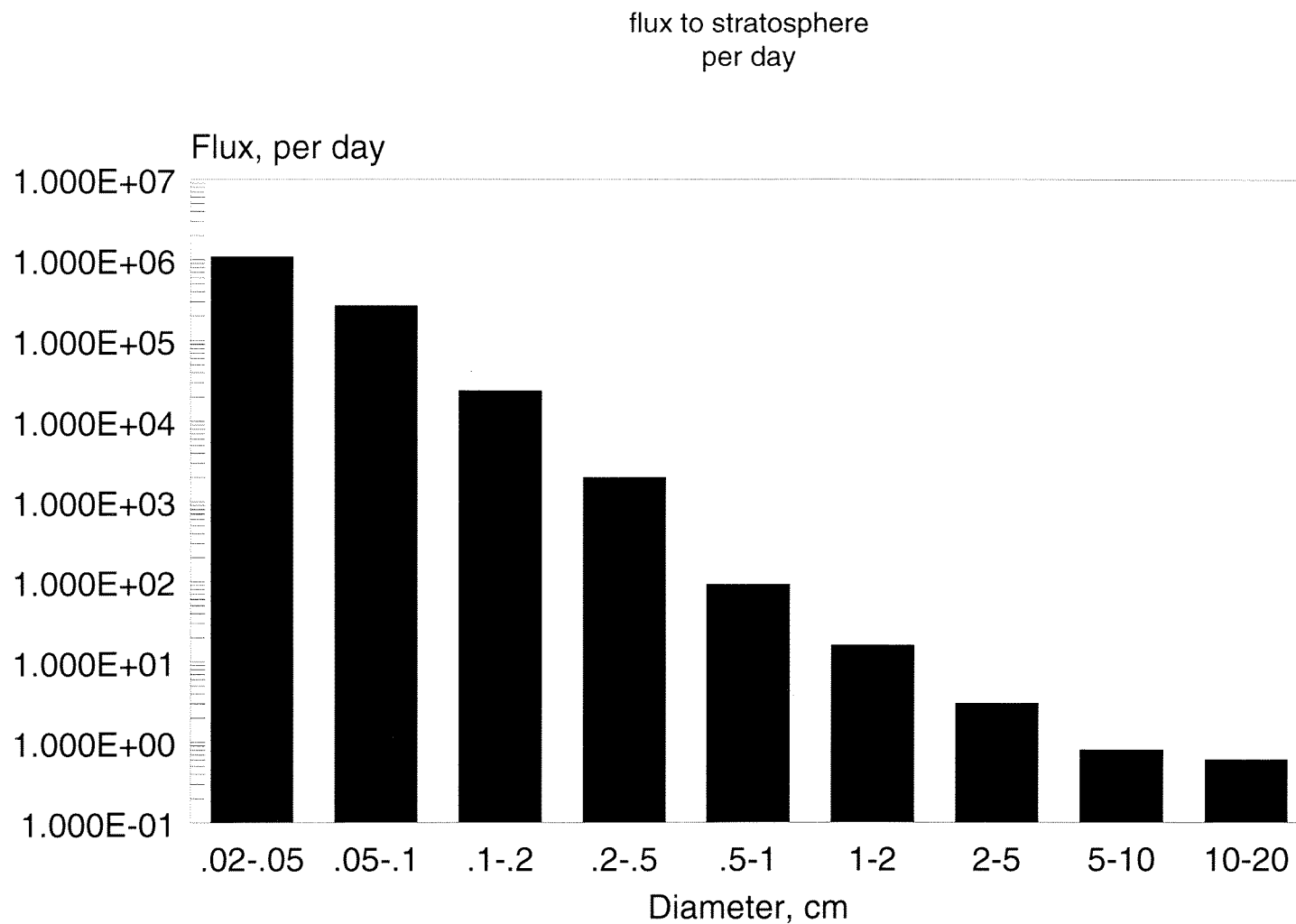
fragmentation) with the orbital decay process. Such a complete model is beyond the scope of this project and thus we take the available estimates of object population and size/mass distribution and subject these objects to the orbital decay process. We have used average material density estimates from Reference 2.3 for our decay analysis:

- o 4.0 g/cm^3 for diameter less than or equal to 0.62 cm,
- o $2.8 d^{-0.74} \text{ g/cm}^3$ for diameter greater than 0.62 cm (d in cm).

A spherical geometry is assumed. The density of larger objects is reduced to account for irregular shapes such as hollow structures.

The deorbit time (time for the object to reach 50 km as a result of atmospheric drag) was calculated for objects initially at altitudes from 200 to 1200 km and for sizes from 0.0001 to 100 cm. The calculation was made assuming a solar radio flux index of 150 (which is about an average value, which results in about an average atmospheric density, which results in an average estimate of drag, and which predicts an average estimate of orbital decay time) and is based on the present 1994 object density (and hence should have a growth factor applied for later years). The calculations are conservative (smaller decay time) in that circular orbits were assumed.

The resulting flux into the stratosphere is given in Figure 2.3 as a function of object size. The flux is constructed by combining deorbit times from altitudes from 200 km to 1200 km and for object sizes from 1 μm to 100 cm. While an object is in orbit the decay rate is directly proportional to the weight to drag ratio of the object: large objects take longer to deorbit than do smaller objects. When the object enters the stratosphere and begins the



based on 1994 data; zero growth

Figure 2.3. Orbital Debris Flux to the Stratosphere

reentry process aerodynamic drag decelerates smaller objects more than the larger objects.

The resultant effect is that the population of debris in the stratosphere will be biased toward the smaller objects. The population of smaller objects in the stratosphere will be further increased by several mechanisms:

- object breakup as a result of the reentry process;
- stripping of particulates from the surface of larger objects by aerodynamic drag during deorbit-approximately 10^6 - 10^7 micrometer-sized particles per square foot are attached to an orbiting object with, perhaps, thousands of square feet of area per spacecraft (Ref. 2.5);
- potential solidification of small droplets (produced from melting/ablating during reentry);
- particulates in materials such as paints that are released when binder materials melt during reentry heating (Ref. 2.6).

3. Reentry Mechanics and Heating of Deorbiting Debris

Understanding the reentry of the orbital debris objects requires consideration of several effects:

- 1) deorbit conditions (at about 120 km);
- 2) reentry trajectory;
- 3) aerodynamic heating;
- 4) heating of the debris object and possible melting or vaporization.

The evaluation is further complicated by the myriad of debris sizes, shapes, and materials.

Reentry trajectories are calculated using a three degree-of-freedom trajectory analysis.

The initial conditions for the analysis were chosen as the orbital velocity at 120 km, 7825 m/s. A range of initial flight path angles were considered. A key component to the trajectory determination is assessment of the drag coefficient. We have used drag coefficients applicable to spherical (or near-spherical) objects as well as tumbling drag coefficients for cylindrical-like objects (we should be very clear here and point out that we must treat representative rather than specific object shapes). The actual drag coefficient is "bridged" between the free-molecule value and the continuum value (transitional flow regime). Bridging is necessary to make reentry analyses tractable. We have based our bridging functions on evaluation of data and analysis for various blunt bodies (References 3.1 & 3.2).

Sample drag coefficients for continuum and free-molecule flow are:

Object Type	Continuum Drag Coefficient, C_C	Free-Molecule Drag Coefficient, C_{FMF}
Sphere	0.9	2.1
Tumbling cylinder	1.05	2.4

The bridging function used for drag is

$$\phi = Kn/(Kn + 0.3).$$

where the Knudsen number is the free stream, ambient, mean free path divided by the appropriate reference length (e.g., the sphere diameter).

The drag coefficient is thus constructed by

$$C_D = C_C + \phi(C_C - C_{FMF}).$$

The drag entered into the equations of motion is thus

$$\frac{1}{2} \rho V^2 \times Area \times C_D$$

where ρ is the ambient density,

V is the vehicle velocity,

and $Area$ refers to the object reference area.

The aerodynamic heating is also characterized by a bridging function (except for small Knudsen numbers e.g., $Kn < 0.05$). The bridging function for stagnation point heat transfer is:

$$\phi = Kn/(Kn + 0.1).$$

The continuum value for stagnation point heat transfer is (Refs. 3.3, 3.4, 3.5, 3.6)

$$q_{stag} = \frac{3 \times 10^{-5} \sqrt{\rho} \times V^{3.26}}{\sqrt{R}}, \quad W/m^2$$

where ρ is ambient density in kg/m^3 ,

V is debris velocity in m/s ,

and R is the effective radius of the debris object, in meters.

Heating of the reentering debris object is a balance of aerodynamic heating and heat loss by radiation. The radiant heat loss by the object was assumed to be to a 300K sink (earth) over one half of the object surface area and to a 0K sink (space) over the remaining half of the objects area. A surface emissivity of 0.8 is assumed:

$$q_{rad} = 0.8 \times 5.67 \times 10^{-8} \times (T_{wall}^4 - \frac{1}{2} 300^4), \quad W/m^2$$

The stagnation point heat transfer is experienced only near the objects stagnation point. The stagnation value is averaged over the object surface in order to account for the tumbling motion of the vehicle and for the localized high stagnation heating. Guidelines for this averaging are given by Cropp (Reference 3.2) for several shapes. As an example, for a sphere the freestream heat flux is multiplied by a factor of 0.275 while the continuum value is multiplied by 0.25.

Trajectory/heating assessments were made for a collection of object sizes, shapes, and materials. The temperature of the reentering debris object was calculated by evaluation of the net heating of the object and the thermal mass (capacity) of the object. A result of particular interest was the altitude at which the melting temperature of the object was reached: at this point the debris object is expected to breakup into droplets and/or vaporize and the reentry process will cease. A second result of interest is the altitude where the object temperature reaches 450 K. At approximately 450K paints, epoxies, resins, and other composite materials will decompose with the possibility of formation of NO_x and the subsequent depletion of ozone.

Physical properties for selected materials are given in the following table:

material	density, kg/m ³	specific heat, cal/gm/K	melting point, K	thermal conductivity, W/m/K
Aluminum	2700	.22	870	240
Beryllium	1850	.44	1560	220
Stainless Steel	7800	.10	1500	45
Titanium	4500	.12	1930	20
Magnesium	1740	.24	870	160

The deorbiting/heating process is a balance of the drag and mass which determines the velocity/altitude state vector of the deorbiting event. The velocity/mass and object geometry determines the heating rate. The thermal capacity of the object along with the heating history determines the object temperature. And, finally, the object melting point is an important factor which determines whether or not the object deorbits, melts or evaporates, or, in the case of a complex object such as a spacecraft breaks up into smaller objects.

A number of calculations were made for objects with the recommended material density,

- 4.0 g/cm³ for diameter less than or equal to 0.62 cm,
- $2.8 d^{-0.74}$ g/cm³ for diameter greater than 0.62 cm (d in cm).

and with the heat capacity of aluminum. These results are shown in Figures 3.1-3.12. The net heat flux to the object (convective-radiative) is plotted along with the material bulk temperature. As the objects encounter the rapidly increasing density with decreasing altitude they began to experience drag (which slows the object) and heating (which increases the objects temperature. The very small particles decelerate rapidly, do not heat significantly, and drift into the stratosphere at a very low velocity (the long time for a very small particle to drift through the stratosphere is shown in Figure 3.13). The very large particles may survive because the thermal mass is sufficient to avoid reaching the melting temperature (and possibly avoid breakups caused by the state of stress set up by the aerodynamic loads- exacerbated by high temperature) *and* because the body is sufficiently blunt to avoid high stagnation point heating (the $R_{nose}^{-0.5}$ effect: a blunt nose reduces stagnation point heating during hypersonic reentry). The intermediate size particles however enter the high density atmosphere with high velocity. They experience high stagnation heating and are heated to relatively high temperature. The intermediate size objects described in Figures 3.3-3.8 reach the melting point of aluminum above the stratosphere. The results obtained the present analysis are consistent with results reported in Reference 3.7 (lower heat flux for smaller objects-lower ballistic coefficient) and Reference 3.8 (reentry survivability of large spherical objects).

Sphere Diameter= 0.001 cm
 @ 122000. m: $v_t=7673$. km/s
 and $\gamma=0.0$

17

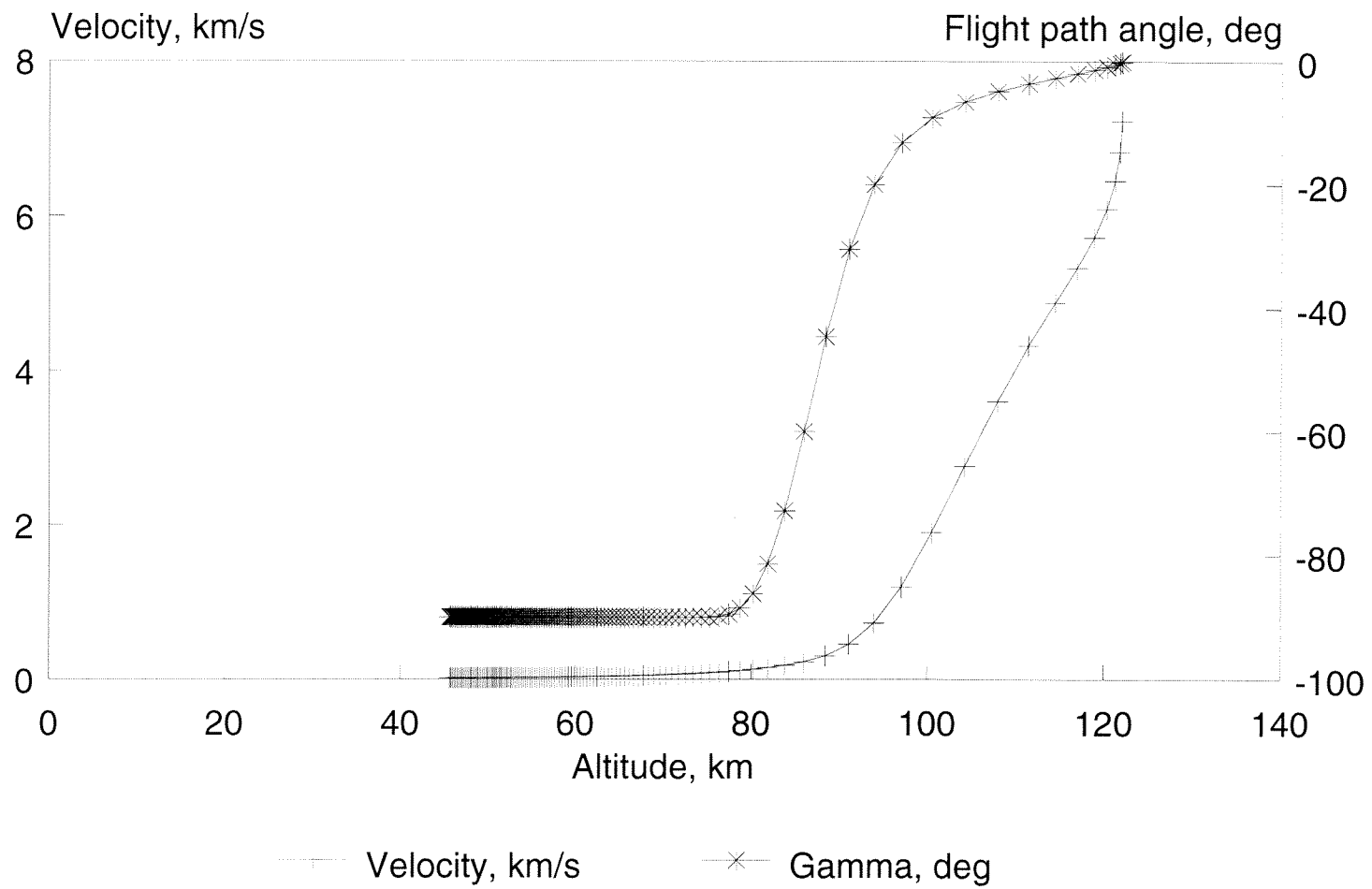


Figure 3.1.

Aluminum: recommended density

Sphere Diameter= 0.001 cm
@ 122000. m: vt=7673. km/s
and gamma= 0.0

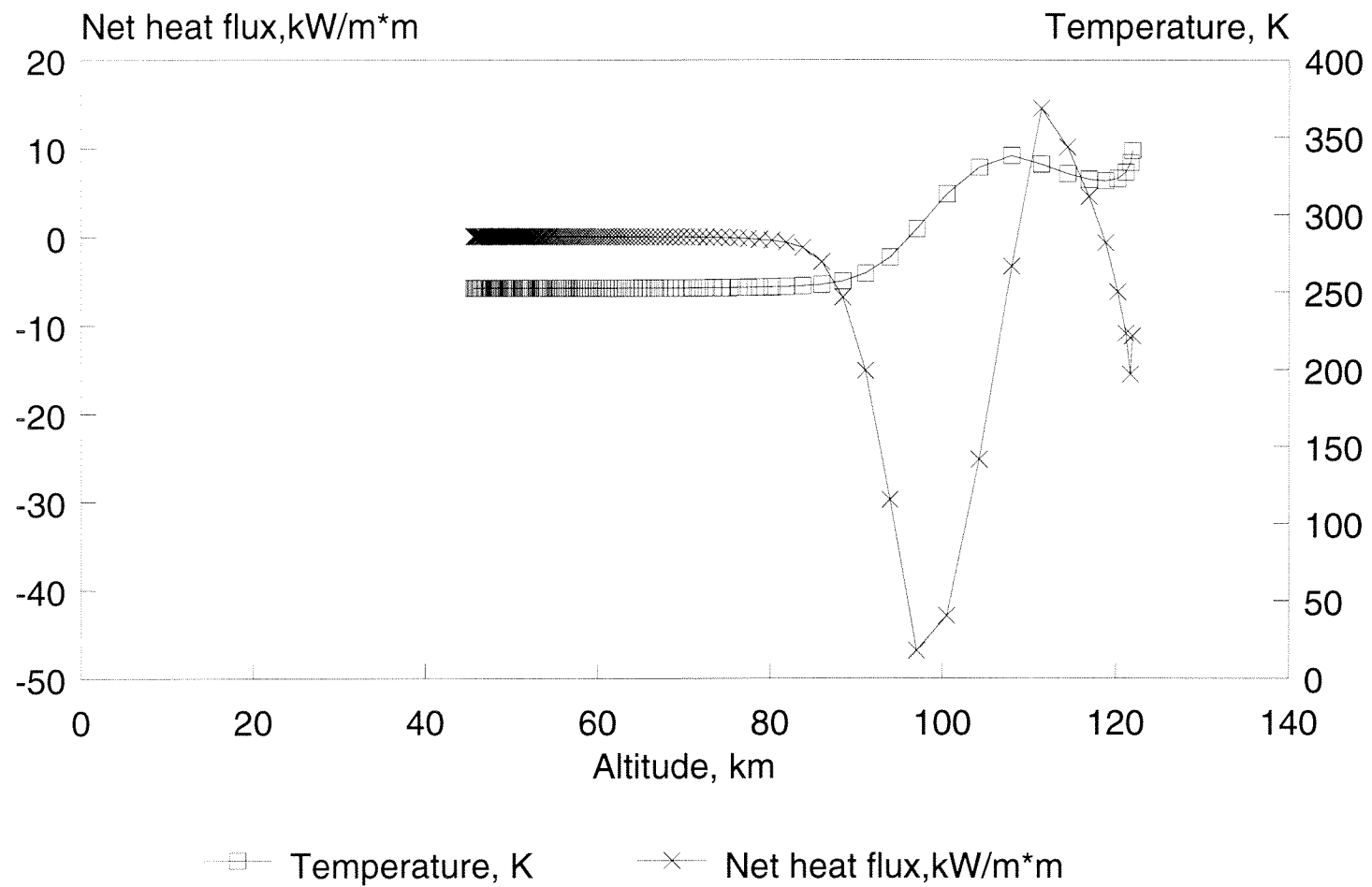


Figure 3.2.

Aluminum: recommended density

Sphere Diameter= 0.10 cm
 @ 122000. m: $v_t=7673$. km/s
 and $\gamma=0.0$

19

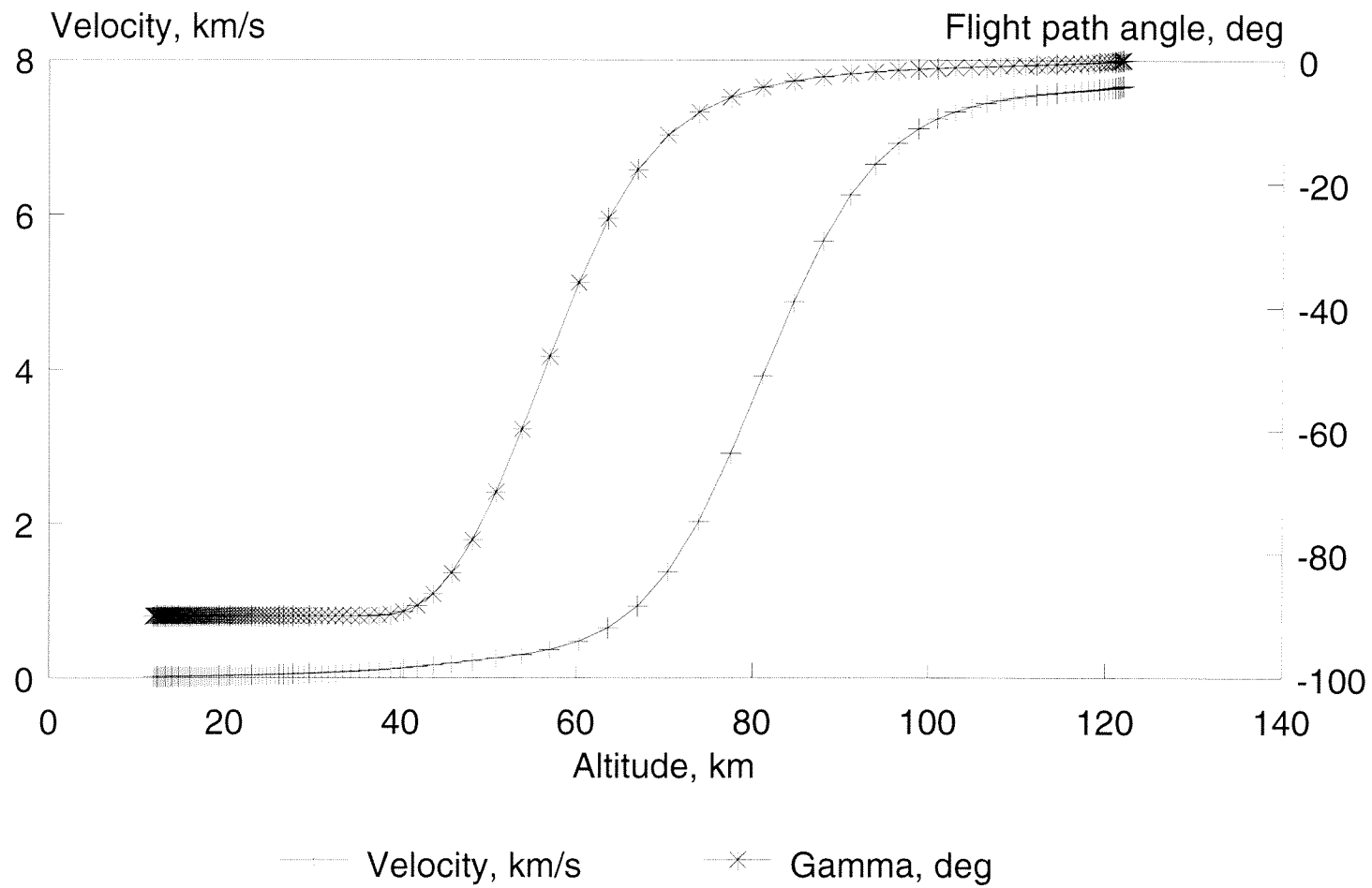


Figure 3.3

Aluminum: recommended density

Sphere Diameter= 0.10 cm
 @ 122000. m: $v_t=7673$. km/s
 and $\gamma=0.0$

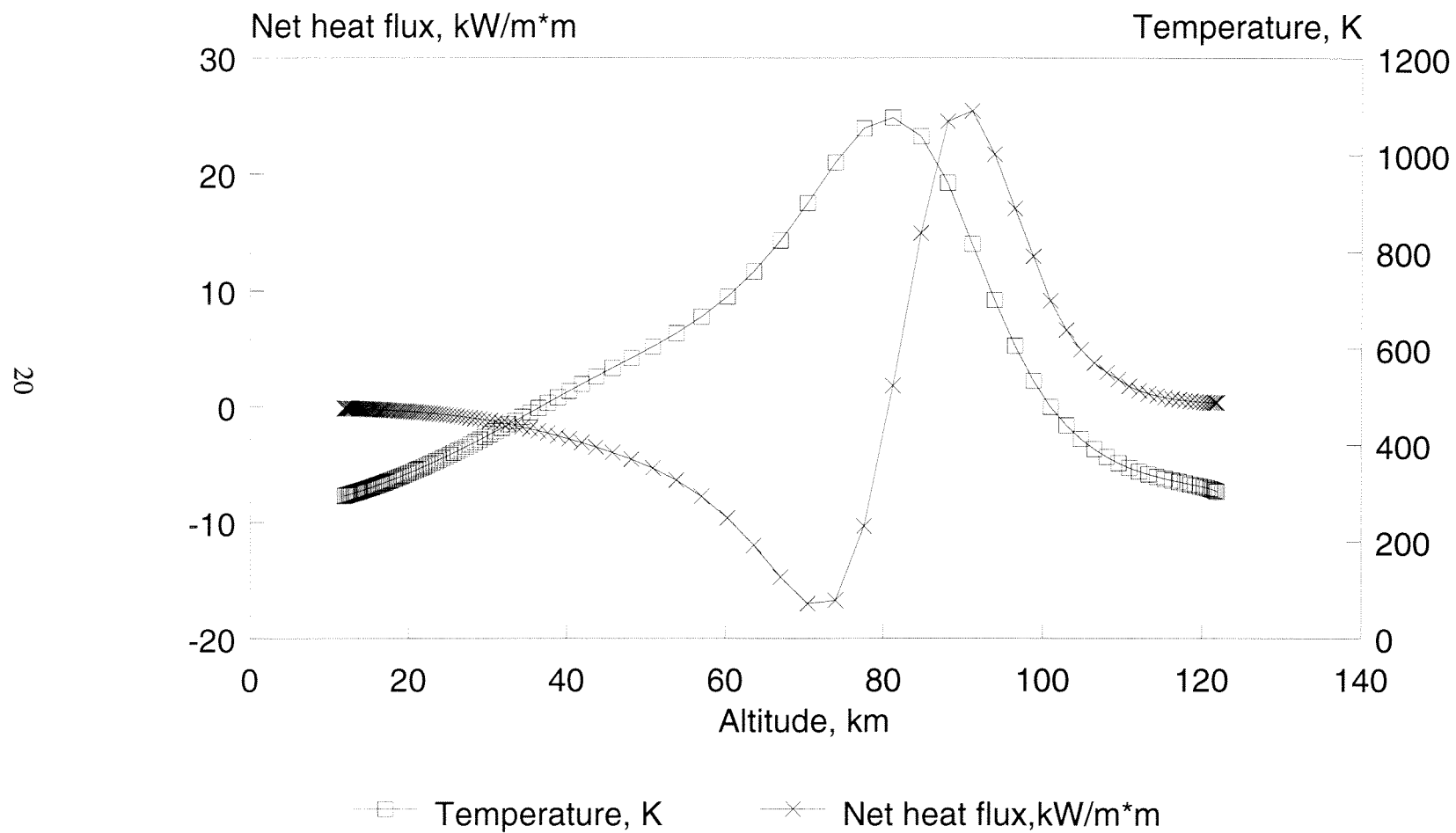


Figure 3.4

Aluminum: recommended density

Sphere Diameter= 1.00 cm
 @ 122000. m: vt=7673. km/s
 and gamma= 0.0

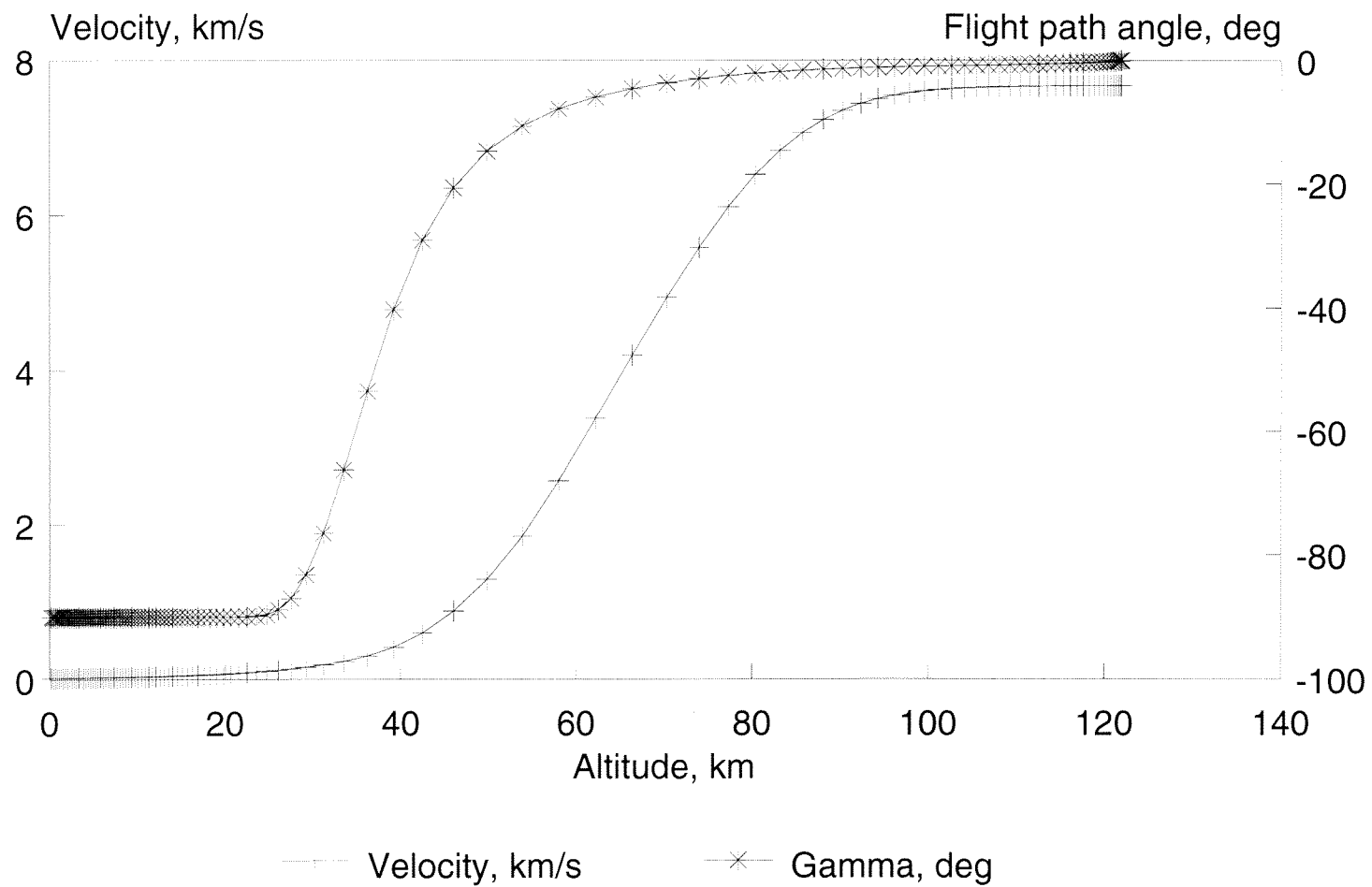


Figure 3.5.

Aluminum: recommended density

Sphere Diameter= 1.0 cm
 @ 122000 m: $v_t=7673$ km/s
 and $\gamma=0.0$

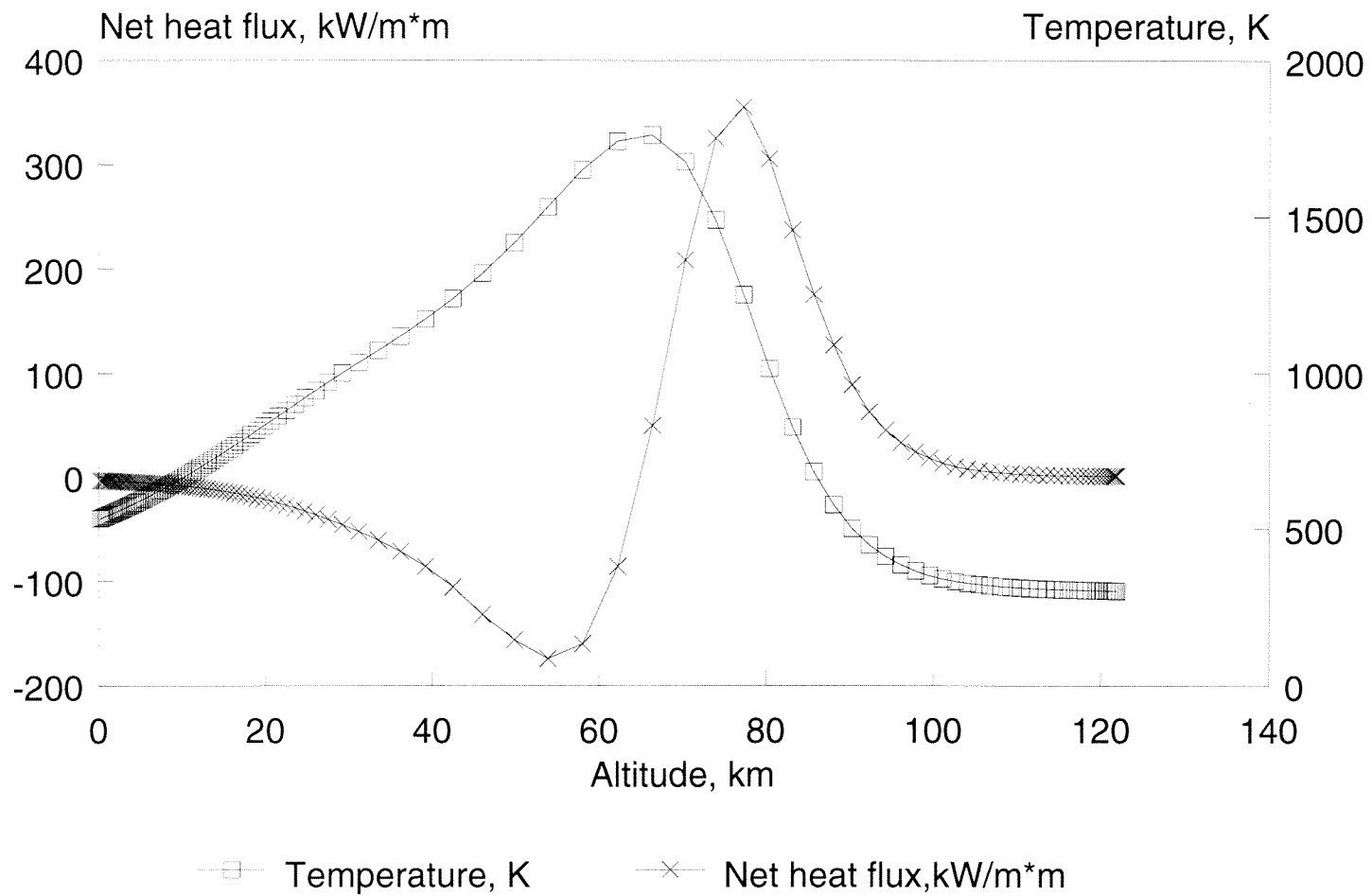
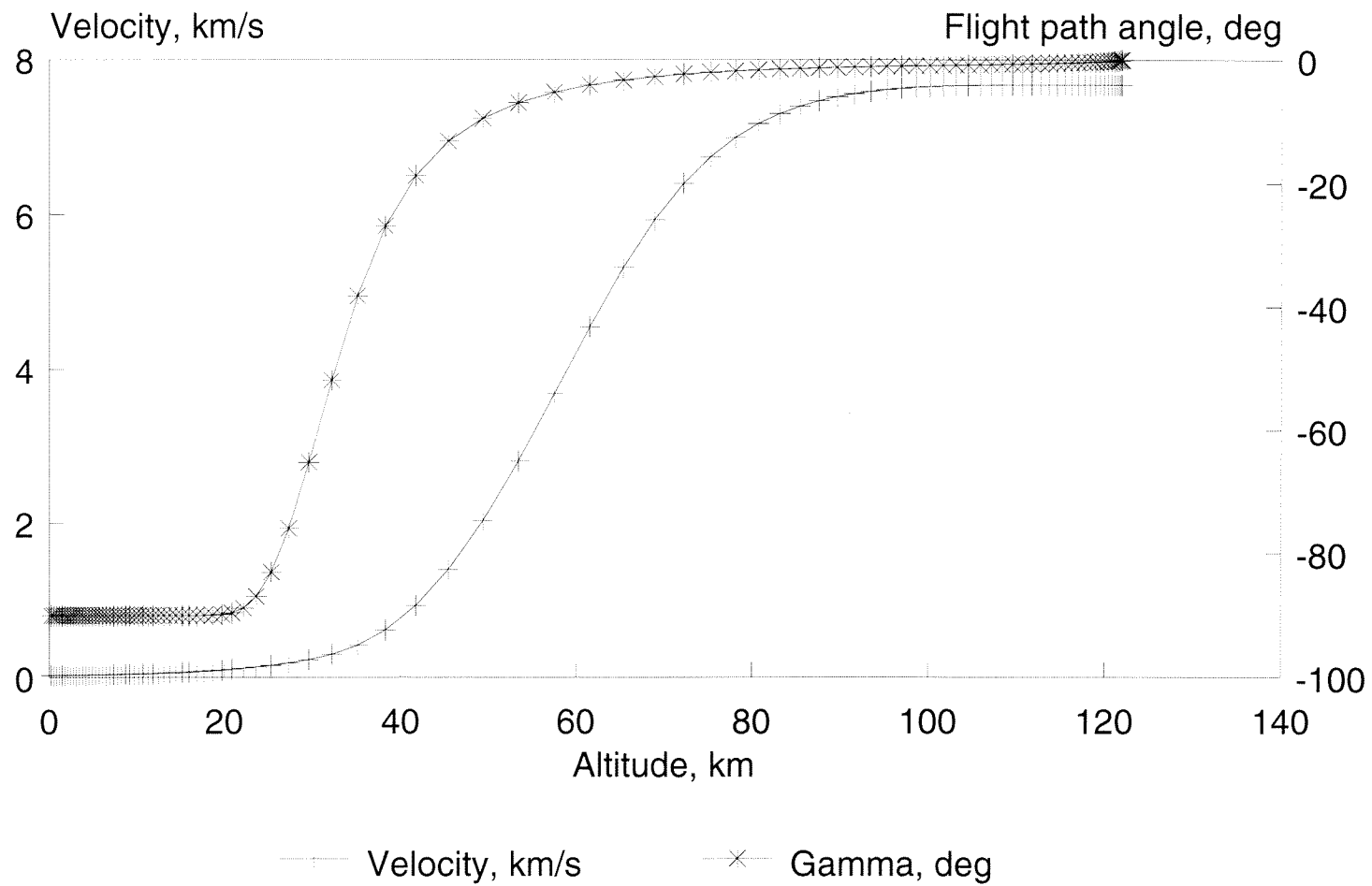


Figure 3.6.

Aluminum: recommended density

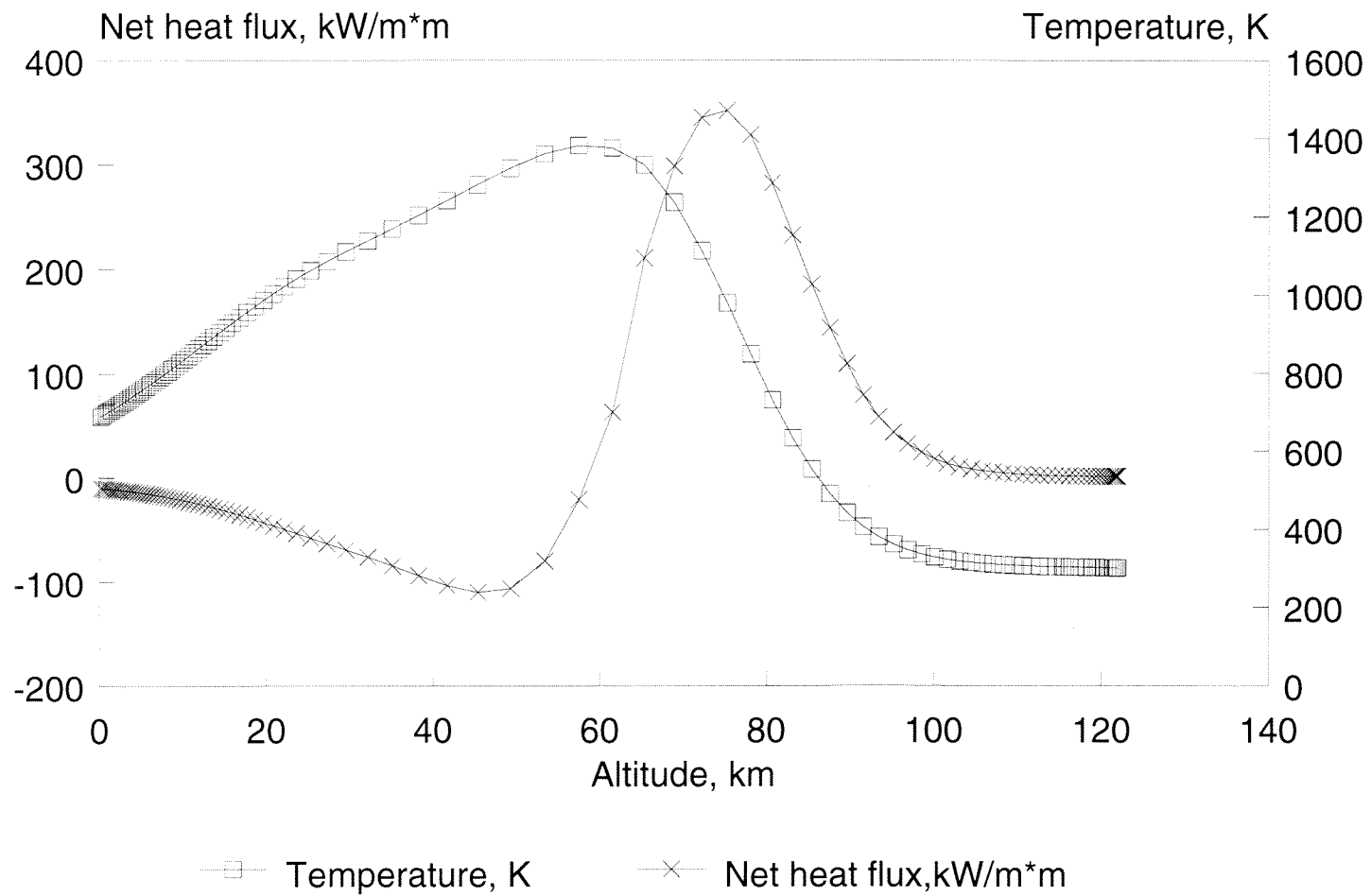
Sphere Diameter= 10.00 cm
@ 122000. m: $v_t=7673$. km/s
and $\gamma=0.0$



Aluminum: recommended density

Figure 3.7.

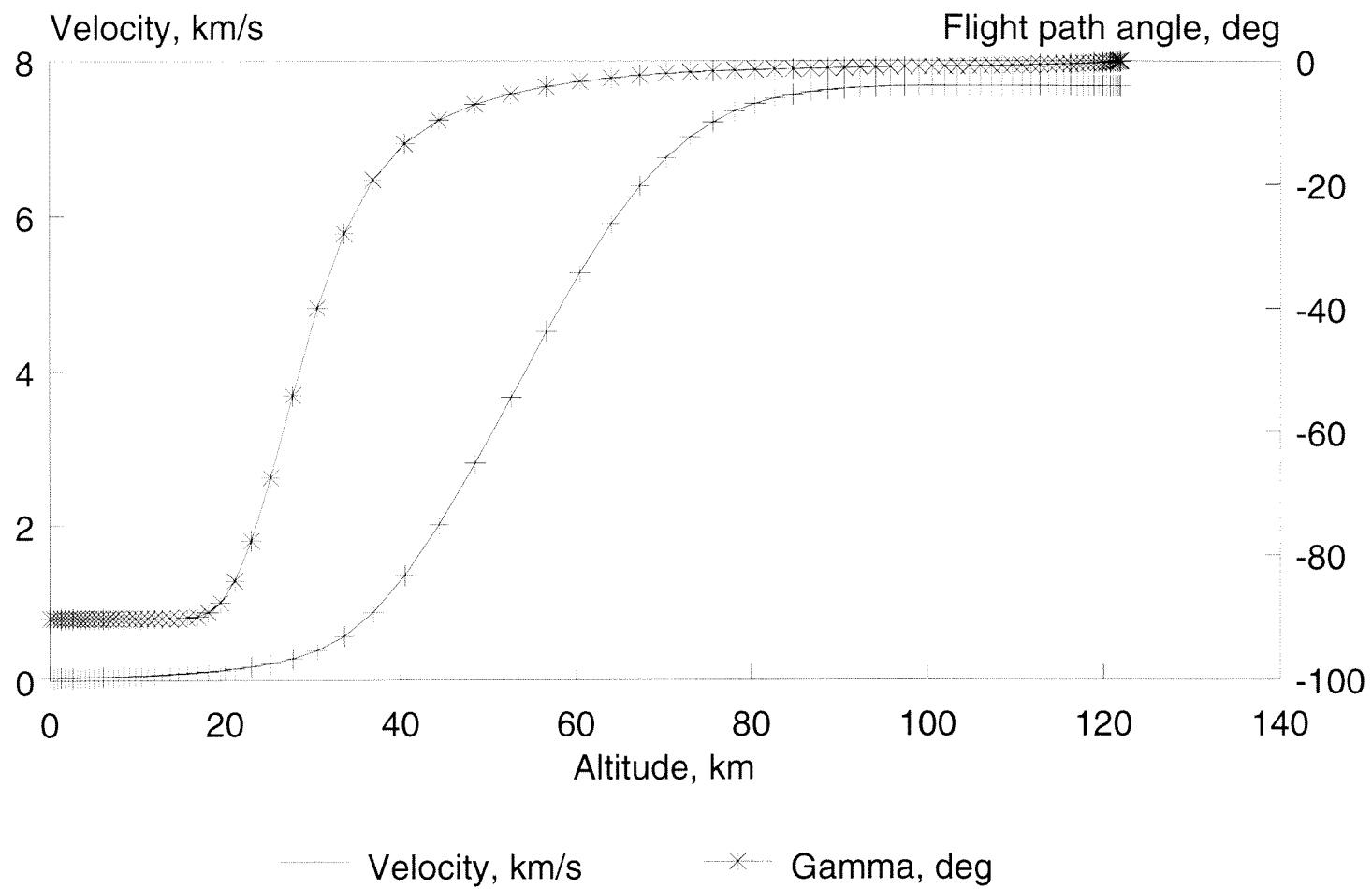
Sphere Diameter= 10.00 cm
 @ 122000. m: vt=7673. km/s
 and gamma= 0.0



Aluminum: recommended density

Figure 3.8.

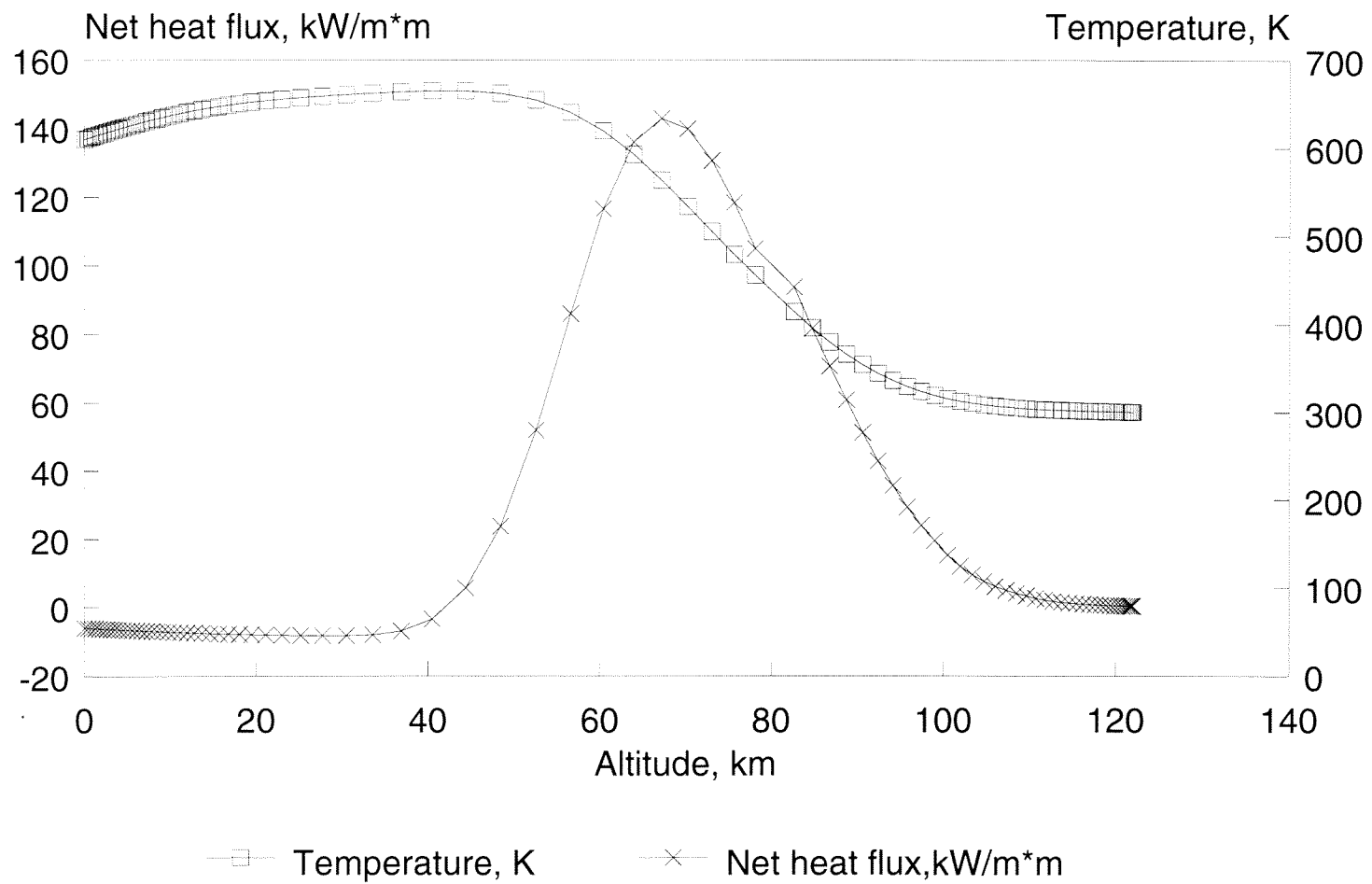
Sphere Diameter=100.00 cm
@ 122000. m: vt=7673. km/s
and gamma= 0.0



Aluminum: recommended density

Figure 3.9

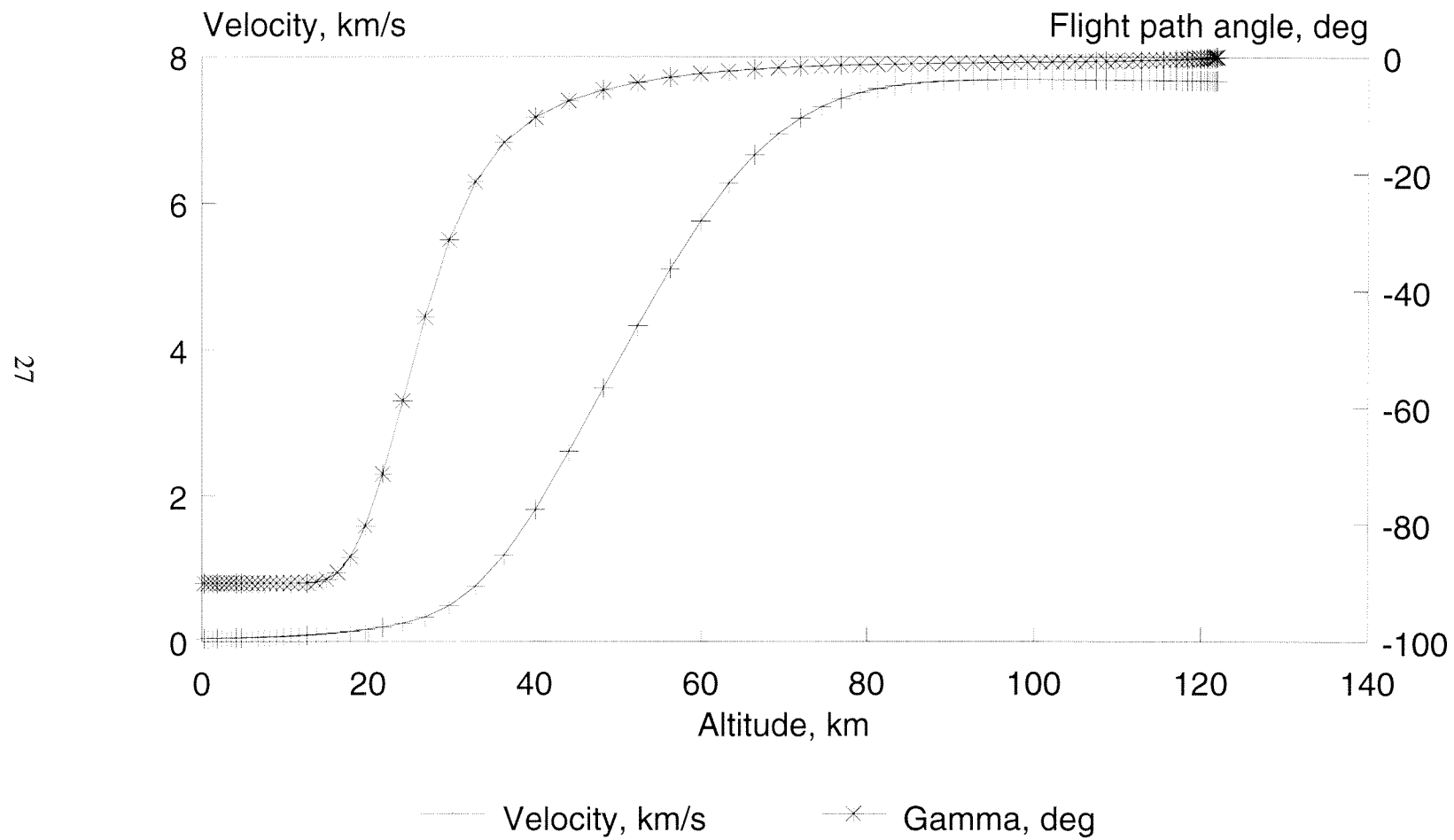
Sphere Diameter=100.00 cm
 @ 122000. m: vt=7673. km/s
 and gamma= 0.0



Aluminum: recommended density

Figure 3.10.

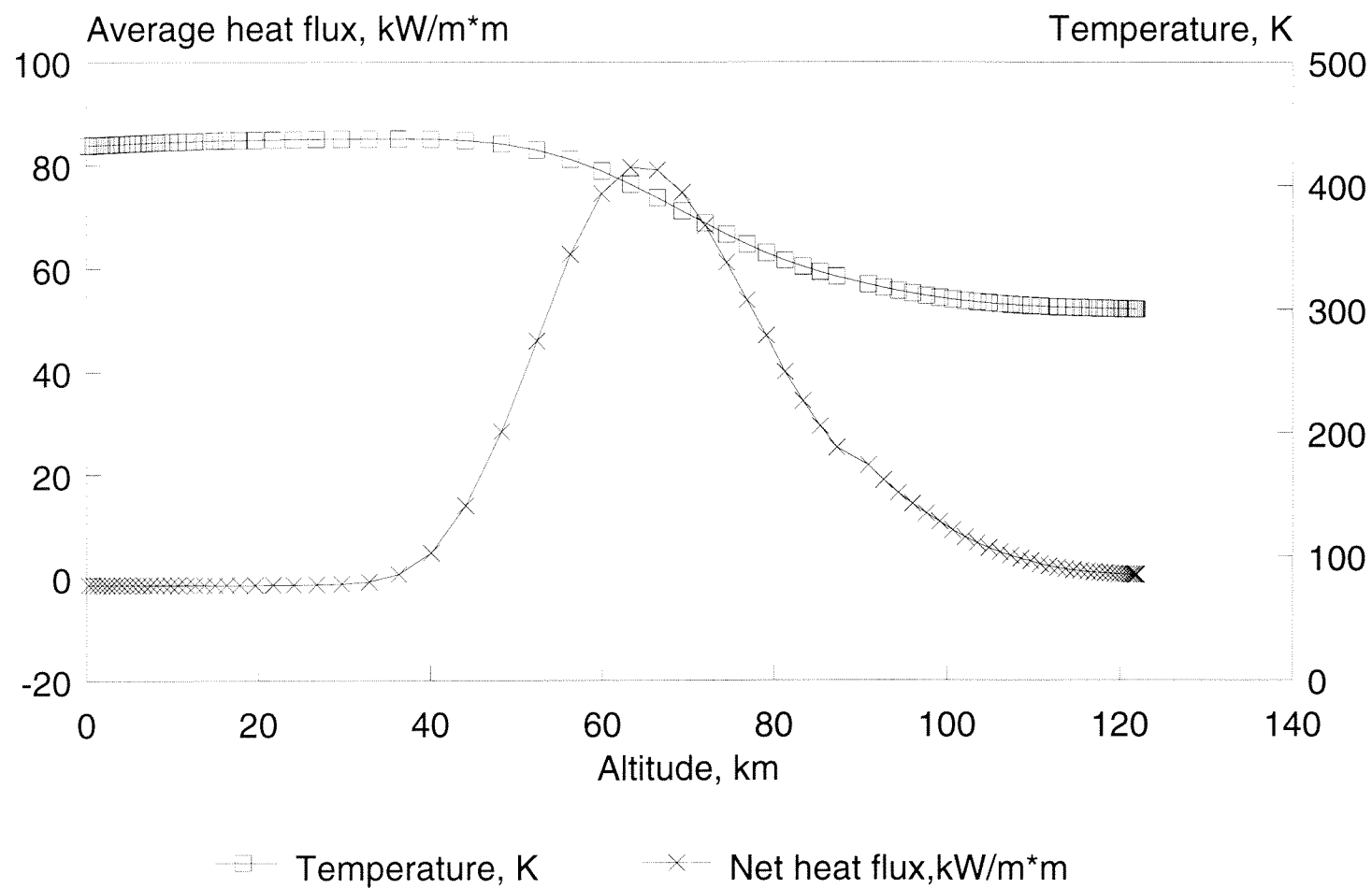
Sphere Diameter=500.00 cm
@ 122000. m: vt=7673. km/s
and gamma= 0.0



Aluminum: recommended density

Figure 3.11.

Sphere Diameter=500.00 cm
 @ 122000. m: vt=7673. km/s
 and gamma= 0.0



Aluminum: recommended density

Figure 3.12.

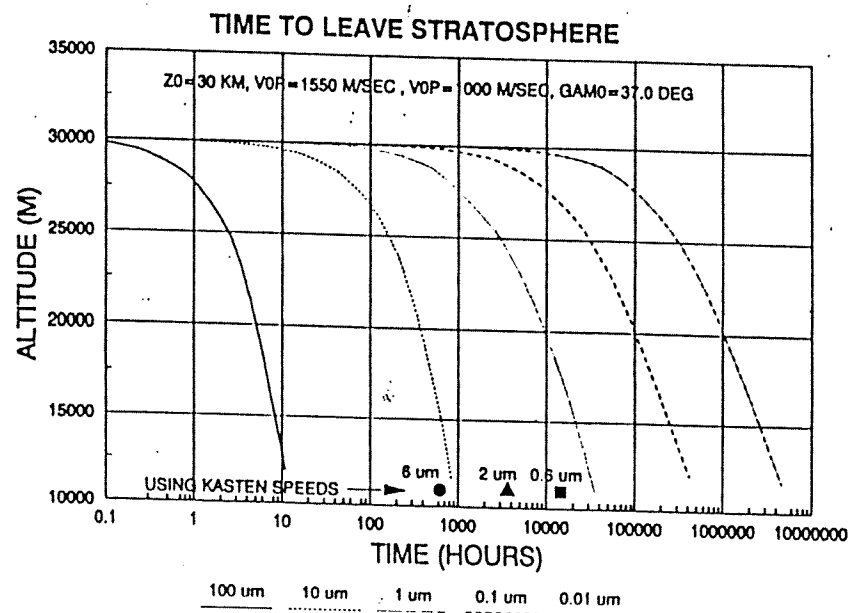
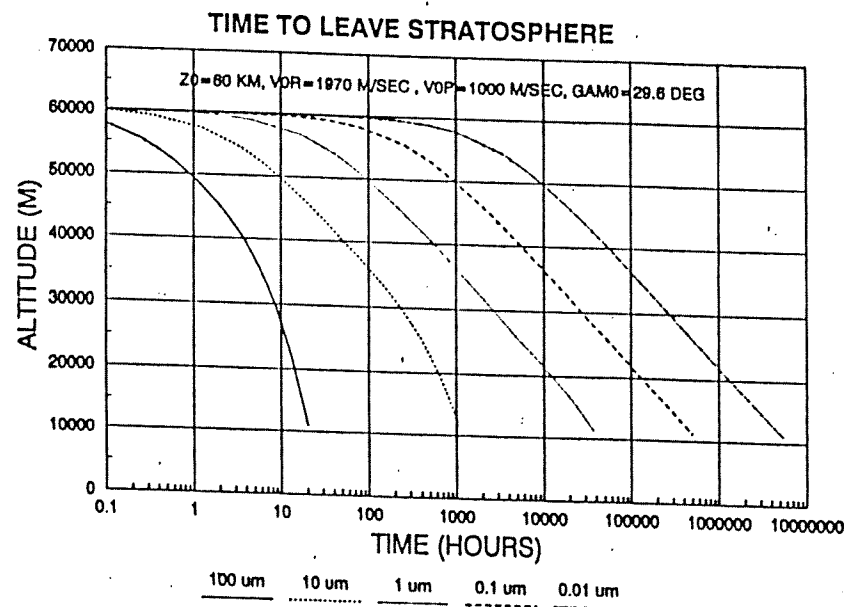


Figure 3.13.

Reentry/heating of several selected objects lead to the following conclusions:

ALUMINUM

- o intermediate size objects (about a 1 cm size) vaporize above the stratosphere
- o extremely small objects (e.g., 10μ) lose momentum rapidly and drift slowly into the stratosphere
- o solid objects ($d > 30$ cm) survive to the earth's surface and reach 450K temperature at 45 km

STAINLESS STEEL

- o reach 450K above the stratosphere
- o smaller particles ($d < 0.1$ cm) are decelerated rapidly at higher altitudes and enter the stratosphere at very low descent velocity
- o larger solid objects ($d > 10$ cm) survive to the earth's surface while the intermediate size objects melt either above or in the stratosphere

BERYLLIUM

- o most beryllium objects survive to the earth's surface - beryllium has a large thermal mass or capacity (ρc) and a high melting point
- o beryllium objects heat to 450 K above the stratosphere

MAGNESIUM

- o magnesium objects larger than about 20 cm survive to the earth's surface
- o all size magnesium objects reach 450 K above the stratosphere.

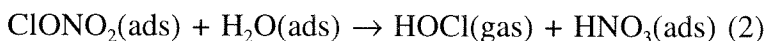
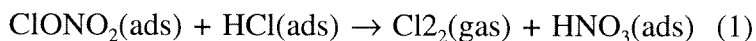
The above results summarize deorbit characteristics for a large number of debris materials, shapes and sizes. It was beyond the scope of this project to either characterize every possible debris material, shape, and size or to characterize the heating and breakup of entire spacecraft. The deorbit characterization provides guidance for estimation of the initial conditions for examination of the capability of deorbiting debris to destroy stratospheric ozone.

4. Depletion of Stratospheric Ozone by Heterogeneous Mechanisms

This section discusses results of an analysis of the depletion of stratospheric ozone caused by heterogeneous reactions taking place on the surface of deorbiting debris particles as well as resident particles. The particles are assumed to be solid Al_2O_3 (i.e., porosity is zero).

This assumption may be relaxed to include other reentry debris particles since the kinetic rate constant is expected to be similar to that measured for Al_2O_3 particles. We also limit our attention to the smallest debris objects because the heterogeneous reaction rate is controlled by the surface area of the particles which favors the smaller particles on a unit mass basis. We have focused on the micron size particle. We calculate approximately 10^{14} - 10^{15} 1-10 μ size particles entering the stratosphere per day as opposed to about 10^5 particles per day for 1mm size objects and 10 μ size objects have about two orders of magnitude more area than the larger, 1mm, particles.

Historically, the role of heterogeneous reactions associated with stratospheric ozone depletion was considered small compared with the gas phase photochemical reactions. However the observations by Farman et al. (Ref. 4.1) have revealed depletions of total atmospheric ozone content in Antarctica. They observed that a total ozone significantly decreased smoothly over a period from 1975 to 1985, but it only occurred in the spring seasons. The mechanism by which ozone is depleted during this period is now commonly considered to be associated with the following heterogeneous reactions involving the reservoir gaseous molecules containing chlorine and the surrounding polar stratospheric clouds consisting of ice particles (Refs. 4.2 & 4.3)



where (ads) stands for adsorbed. Photodissociation of Cl_2 and breakdown of HOCl to form radicals Cl and OH subsequently depletes ozone.

It has been speculated that deorbiting debris entering from high altitude can break up and form numerous smaller particles which in turn can provide active sites for heterogeneous reaction similar to those postulated for the ice particles of polar stratospheric clouds(PSC). To evaluate the impact of deorbiting debris on stratospheric ozone Professor Mario Molina of the Massachusetts Institute of Technology was contracted to perform experiments which measure the rate parameter in terms of reaction probability (γ) on the surface of Al_2O_3 particles under typical stratospheric conditions (Ref. 4.4) . At 212K and partial pressures of 7.56×10^{-7} torr, 8.33×10^{-8} torr and 4.41×10^{-4} torr for ClONO_2 , HCl and H_2O respectively, the reaction probability for the disappearance of ClONO_2 (or the production of Cl_2) was found to be $\gamma=0.014$. Thus, the measured heterogeneous rate associated with Al_2O_3 is seen to be approximately one order of magnitude slower than that associated with the PSC (Ref. 4.5).

4.1 ANALYSIS METHOD

The model we have designed for the evaluation of ozone depletion in the stratosphere due to deorbiting debris is based on a steady one-dimensional (in radial direction) diffusion of reacting reservoir gas ClONO_2 to the surface of a single particle on which chemical reactions

between ClONO_2 and HCl take place to generate Cl_2 gas. In order to obtain a close form solution a stagnant environment is further assumed (the issue of ClONO_2 conversion enhancement due to convection will be addressed in the following). It should be noted that the model considers equal importance between diffusion and chemical reaction. Therefore the governing equation is

$$\frac{d}{dr} 4\pi r^2 D \frac{dC_A}{dr} = 0 \quad (3)$$

where r , D and C_A stand for radial location, diffusion coefficient and ClONO_2 concentration. With proper boundary conditions (i.e., mass flux $= (1/4)\gamma \bar{C} C_A$ and the specification of farfield species concentration) the concentration profile can be shown to be

$$C_A = C_{A_\infty} e^{(-ar)} \quad (4)$$

where C_{A_∞} is the ambient concentration of ClONO_2 , $a \equiv \gamma \bar{C} S / (16\pi D)$, and $\bar{C} (= \sqrt{8kT/\pi m})$ and S are, respectively, the molecular speed of ClONO_2 and surface area of an Al_2O_3 particle. Therefore the mass consumption rate of ClONO_2 (or production rate of Cl_2) is given as

$$\frac{dm}{dt} = 4\pi r^2 D \left. \frac{dC_A}{dr} \right|_{r=r_p} = (1/4) \gamma \bar{C} S C_{A_\infty} e^{-ar_p} \quad (5)$$

where r_p is the particle radius. Incidentally, the ratio of a/r_p which controls the species concentration decrease towards the particle can be shown as

$$a/r_p = \frac{(1/4)\gamma\bar{C}}{(D/r_p)} \quad (6)$$

which represents the ratio of heterogeneous reaction rate and diffusion rate (Ref. 4.6). Based on a $D=176 \text{ cm}^2/\text{s}$, and $\gamma\bar{C}$ corresponding to partial pressure of ClONO_2 of 10^{-7} torr in the stratosphere (ambient temperature = 226K), the ratio is on the order of 10^{-5} for micron-size particles indicating that heterogeneous reaction rate is slow thus controlling the rate of ozone depletion.

ANALYSIS RESULTS

In order to evaluate the potential ozone depletion caused by heterogeneous reactions on the surface of deorbiting debris particles the particle density must be determined. This is facilitated by using analysis results of debris size distribution and orbital debris flux illustrated in Fig. 2-3 from which the debris density in the stratosphere is calculated as

$$N_p = \frac{dN_p/dt}{vA}$$

313

where $N_p \equiv$ debris density in particle/cm³, $dN_p/dt \equiv$ total number of deorbiting particles per unit time, $v \equiv$ the normal component of the velocity of reentering, $A =$ surface area of the stratosphere. By using

$$dN_p/dt = 10^{15} \text{ particles/day,}$$

$$v = 7.0 \times 10^{-3} \text{ cm/sec}$$

$$A = 5.14 \times 10^{18} \text{ cm}^2$$

the average micron-size class debris density in the stratosphere is calculated. Table 4.1 summarizes the particle density in the stratosphere calculated from the above method from measurements by Zolensky (Ref. 4.7) and Hobbs (Ref. 4.8). The present estimate based on orbital decay/population calculations is consistent with the Zolensky result. A complete characterization of the deposition of micrometer-size particles into the stratosphere by all orbital debris requires evaluation of the production caused by reentry of larger objects (as outlined in Section 2). We restrict our attention to the present result (or the Zolensky data).

Table 4.1 Particle density: number per cm³

Deorbiting Debris	Resident Particles (Zolensky)	Volcanic Ashes (Hobbs)
3.0×10^{-7}	1.0×10^{-6}	1.5×10^4

Using the rate of ClONO_2 disappearance (therefore equals to half the ozone depletion rate) in Equation 5 and the density of particles in Table 4.1, the effect of heterogeneous reaction on stratospheric ozone can be appreciated by evaluating the time required for 1% ozone depletion. Table 4.2 shows the times (in years) for three different sizes of particles.

Table 4.2 Time in years for 1% ozone depletion.

Particle size	1 μm	10 μm^*	100 μm^*
Deorbited debris	3×10^5	3×10^3	30
Resident particles	8×10^4	8×10^2	8.0
Volcanic ashes	5×10^{-6} (167s)	5×10^{-8} (1.67s)	5×10^{-10} (16ms)

* assuming 1 micrometer object density

CONCLUDING REMARKS

Clearly, there is little or no global impact on stratospheric ozone due to either deorbiting debris particles or resident particles according to this analysis (we assume that other particles-e.g., zinc oxide, magnesium oxide-have about the same reactivity as the aluminum oxide particles). The reasons are twofold: slow reaction rate and low particle density. It is noted however, large deposition of particles in the stratosphere due to volcanic eruptions can have a significant impact on the local ozone column density.

5. Depletion of Stratospheric Ozone by Homogeneous Mechanisms

INTRODUCTION

Deorbiting debris may reenter into the stratosphere at hypersonic speed generating gas phase species harmful to ozone. These species are originated from two sources, namely from behind the bow shock where temperature can be as high as 20,000K; and from the pyrolysis of polymeric material commonly found in the heatshield and spacecraft paints. The major specie produced behind the shock, which is also known to destroy ozone is nitric oxide, NO. The pyrolysis gas products which contain hydrocarbon fragments and bound-nitrogen can react with ambient atomic oxygen or oxygen generated from dissociation of molecular oxygen behind the shock, to form species such as hydroxyl radical (OH) and nitric oxide. To evaluate the impact of deorbiting debris on stratospheric ozone the extent of destruction due to homogeneous reactions involving these species was examined.

5.1 ANALYSIS METHOD

To properly evaluate the impact of these species on stratospheric ozone, calculations must be performed to determine the extent of release of these species, and the dispersion or dilution of these species with the ambient air in the form of a wake. The exact calculation for the production of these species would required a reacting flow analysis of a body traveling in hypersonic speeds. A one dimensional, stagnation streamline, reacting flow analysis was used for the analysis since it provides the level of detail required to address the present problem. The thermal nitric oxide production described by the extended Zeldovich mechanism represents the upper

bound estimate because the temperature distribution associated with the stagnation streamline is the highest among all streamlines, and thermal NO production favors high temperatures.

Atmospheric chemistry will have a much longer time scale than the time scales associated with reacting flow in the immediate vicinity of deorbiting debris. This suggests that the ozone-depletion species contained in the wake will disperse without significant chemical reactions taking place. Therefore, to determine if the locally injected NO would create any local effect on ozone, i.e., create a hole in which ozone is greatly reduced, a far wake analysis must be performed to establish the locally diluted NO concentration. The turbulent far wake analysis was done based on the study of a blunt-nosed bodies at hypersonic speeds (Ref. 5.1-5.5). Further assessment of the hypersonic wake determined the following guidelines:

- The object wake (driven by the bow shock) will be dispersed by turbulent diffusion for all but the smallest objects.
- At approximately 1000 body diameters downstream from the object the average wake velocity decreases to about 1% of the object velocity.
- The corresponding wake diameter (for spheres) at 1000 diameters is about five to ten times the body diameter. This diameter is used to start the “cold” wake calculations (the “cold” wake remains above ambient temperature at the center and requires more than 1000 diameters to equilibrate thermally).

When the wake reaches near-ambient conditions it is treated as an axisymmetric plume in which species diffusion, gas phase chemical reactions, and photodissociation involving

wake and ambient species take place. This cold plume analysis is identical to that described for rocket exhaust interaction with the ambient species as reported in Reference 1.1.

5.2 COLD WAKE KINETIC MECHANISM

The results of this cold wake analysis is used to assess the creation of a local ozone hole caused by deorbiting debris, and secondly, to determine the global impact by using the debris flux calculated previously in this report. With the emphasis on nitric oxide, the stratospheric chemistry may be reduced to a set of elementary reactions including the NO catalytic cycle that consumes the 'odd' oxygen (i.e., O_3 and O), the NO null cycle which tends to either tie up the available NO molecules or even produce odd oxygen, the NO holding cycle which converts NO into a reservoir species such as N_2O_5 (thus depriving NO from destroying ozone), and the Chapman ozone mechanism (Ref. 5.6). Without further discussion Table 5.1 summarizes the key reactions and their respective rate constants employed in this analysis.

Table 5.1. Reactions and Rates.

1	$\text{H} + \text{O}_2 + \text{M} = \text{HO}_2 + \text{M}$	$\text{K1} = 9.0\text{E-}32$
2	$\text{OH} + \text{O} = \text{H} + \text{O}_2$	$\text{K2} = 3.8\text{E-}11$
3	$\text{OH} + \text{H}_2 = \text{H}_2\text{O} + \text{H}$	$\text{K3} = 7.3\text{E-}16$
4	$\text{OH} + \text{OH} = \text{H}_2\text{O} + \text{O}$	$\text{K4} = 1.4\text{E-}12$
5	$\text{OH} + \text{OH} + \text{M} = \text{H}_2\text{O}_2 + \text{M}$	$\text{K5} = 8.7\text{E-}31$
6	$\text{OH} + \text{HO}_2 = \text{H}_2\text{O} + \text{O}_2$	$\text{K6} = 1.5\text{E-}10$
7	$\text{OH} + \text{H}_2\text{O}_2 = \text{H}_2\text{O} + \text{HO}_2$	$\text{K7} = 1.4\text{E-}12$
8	$\text{HO}_2 + \text{O} = \text{OH} + \text{O}_2$	$\text{K8} = 7.3\text{E-}11$
9	$\text{HO}_2 + \text{H} = \text{OH} + \text{OH}$	$\text{K9} = 8.\text{E-}11$
10	$\text{HO}_2 + \text{H} = \text{H}_2 + \text{O}_2$	$\text{K10} = 8.8\text{E-}12$
11	$\text{HO}_2 + \text{HO}_2 = \text{H}_2\text{O}_2 + \text{O}_2$	$\text{K11} = 3.3\text{E-}12$
12	$\text{H}_2\text{O}_2 + \text{O} = \text{OH} + \text{HO}_2$	$\text{K12} = 1.9\text{E-}16$
13	$\text{N} + \text{O}_2 = \text{NO} + \text{O}$	$\text{K13} = 1.6\text{E-}18$
14	$\text{N} + \text{NO} = \text{N}_2 + \text{O}$	$\text{K14} = 3.4\text{E-}11$
15	$\text{NO} + \text{O} + \text{M} = \text{NO}_2 + \text{M}$	$\text{K15} = 1.4\text{E-}31$
16	$\text{NO} + \text{HO}_2 = \text{NO}_2 + \text{OH}$	$\text{K16} = 1.1\text{E-}11$
17	$\text{NO} + \text{NO}_3 = \text{NO}_2 + \text{NO}_2$	$\text{K17} = 3.3\text{E-}11$
18	$\text{NO}_2 + \text{O} = \text{NO} + \text{O}_2$	$\text{K18} = 1.1\text{E-}11$
19	$\text{NO}_2 + \text{O} + \text{M} = \text{NO}_3 + \text{M}$	$\text{K19} = 1.6\text{E-}31$
20	$\text{NO}_2 + \text{OH} + \text{M} = \text{HNO}_3 + \text{M}$	$\text{K20} = 6.6\text{E-}30$
21	$\text{NO}_2 + \text{NO}_3 + \text{M} = \text{N}_2\text{O}_5 + \text{M}$	$\text{K21} = 7.8\text{E-}30$
22	$\text{NO}_3 + \text{O} = \text{NO}_2 + \text{O}_2$	$\text{K22} = 1.\text{E-}11$
23	$\text{O} + \text{O}_2 + \text{M} = \text{O}_3 + \text{M}$	$\text{K23} = 1.2\text{E-}33$
24	$\text{O} + \text{O}_3 = \text{O}_2 + \text{O}_2$	$\text{K24} = 8.1\text{E-}16$
25	$\text{H} + \text{O}_3 = \text{OH} + \text{O}_2$	$\text{K25} = 1.7\text{E-}11$
26	$\text{OH} + \text{O}_3 = \text{HO}_2 + \text{O}_2$	$\text{K26} = 2.4\text{E-}14$
27	$\text{NO} + \text{O}_3 = \text{NO}_2 + \text{O}_2$	$\text{K27} = 4.2\text{E-}15$
28	$\text{NO}_2 + \text{O}_3 = \text{NO}_3 + \text{O}_2$	$\text{K28} = 2.5\text{E-}18$
29	$\text{OH} + \text{HNO}_3 = \text{H}_2\text{O} + \text{NO}_3$	$\text{K29} = 7.6\text{E-}15$
30	$\text{SO} + \text{O}_2 = \text{SO}_2 + \text{O}$	$\text{K30} = 5.4\text{E-}18$
31	$\text{SO} + \text{O}_3 = \text{SO}_2 + \text{O}_2$	$\text{K31} = 2.4\text{E-}14$
32	$\text{SO}_2 + \text{OH} + \text{M} = \text{HSO}_3 + \text{M}$	$\text{K32} = 1.3\text{E-}30$
33	$\text{HSO}_3 + \text{O}_2 = \text{HO}_2 + \text{SO}_3$	$\text{K33} = 4.\text{E-}13$
34	$\text{SO} + \text{NO}_2 = \text{SO}_2 + \text{NO}$	$\text{K34} = 1.4\text{E-}11$
35	$\text{SO} + \text{OH} = \text{SO}_2 + \text{H}$	$\text{K35} = 8.6\text{E-}11$
36	$\text{SO}_2 + \text{O} + \text{M} = \text{SO}_3 + \text{M}$	$\text{K36} = 4.6\text{E-}34$
37	$\text{H}_2\text{O}_2 + \text{h}\nu = \text{OH} + \text{OH}$	$\text{K37} = 1.6\text{E-}5$
38	$\text{N}_2\text{O}_5 + \text{h}\nu = \text{NO}_3 + \text{NO}_2$	$\text{K38} = 5.\text{E-}4$
39	$\text{NO}_2 + \text{h}\nu = \text{NO} + \text{O}$	$\text{K39} = 8.\text{E-}3$
40	$\text{HNO}_3 + \text{h}\nu = \text{OH} + \text{NO}_2$	$\text{K40} = 1.6\text{E-}5$

5.3 VALIDATION OF KINETIC MODEL

Following the launching of a Titan rocket plume measurements of NO and ozone concentrations at two different times in the troposphere were reported by Steward and Gomberg (Ref. 5.7). The measurements indicate a definite ozone depletion in the presence of NO that was generated from the rocket combustion process (Figure 5.1). Taking the ambient species concentrations at 7 km from U.S. Standard Atmosphere (1976) as the initial condition for the cold plume analysis, and using a turbulent diffusion coefficient appropriate for the troposphere (Ref. 5.8), the kinetic model predicts the presence of an ozone hole with size and magnitude of depletion similar to that of measurements at approximately the same time. Figures 5.2 and 5.3 show the results of this calculation. Figure 5.2 shows the centerline species profiles as a function of time. It can be seen that the ozone, which was initially displaced, begins to show up at the centerline at about 100 seconds and it takes almost 24 hours to return to the ambient level. Figure 5.3 shows the fraction of unconsumed ozone as a function of time with radial location as a parameter. The existence of the ozone hole is demonstrated. Figures 5.4 shows a plume radius of approximately 300 meters at 10 minutes as compared to about 500 meters at $t+5$ minutes in the data. The centerline value computed corresponds to about 3 ppb as compared to the data which shows about 6 ppb. Figure 5.5 shows a radius of about a 1500 meters at 84 minutes as compared to 900 meters at $t+34$ min. in the data. The computed centerline value corresponds to about 20 ppb as compared to about 12 ppb at the somewhat earlier time in the data.

The comparison with the Steward and Gomberg measurements show the relevance and accuracy of the plume/wake dispersion-kinetics model used in this study. The calculation,

however, confined attention to the effects of NO on ozone. The Titan SRM exhaust will contain chlorine as well as NO. It should be noted, however, that the NO₂ photodissociation, an important reaction in the NO catalytic cycle, takes place in the solar spectrum between 200-700 nm while Cl₂ or ClO photodissociation takes place at 240-310 nm (Ref. 5.9). The solar flux in the lower troposphere at 200-700 nm is, orders of magnitude higher than that in the 240-310 nm regime (Ref. 5.10). It is therefore anticipated that the chlorine catalytic cycle is not as important as the NO cycle in the lower troposphere. The ozone hole observed was quite likely caused by the presence of the nitric oxide in the Titan SRM exhaust. This contention should, as a follow-on activity, be verified by performing a complete cold plume calculation with both chlorine and NO mechanisms included.

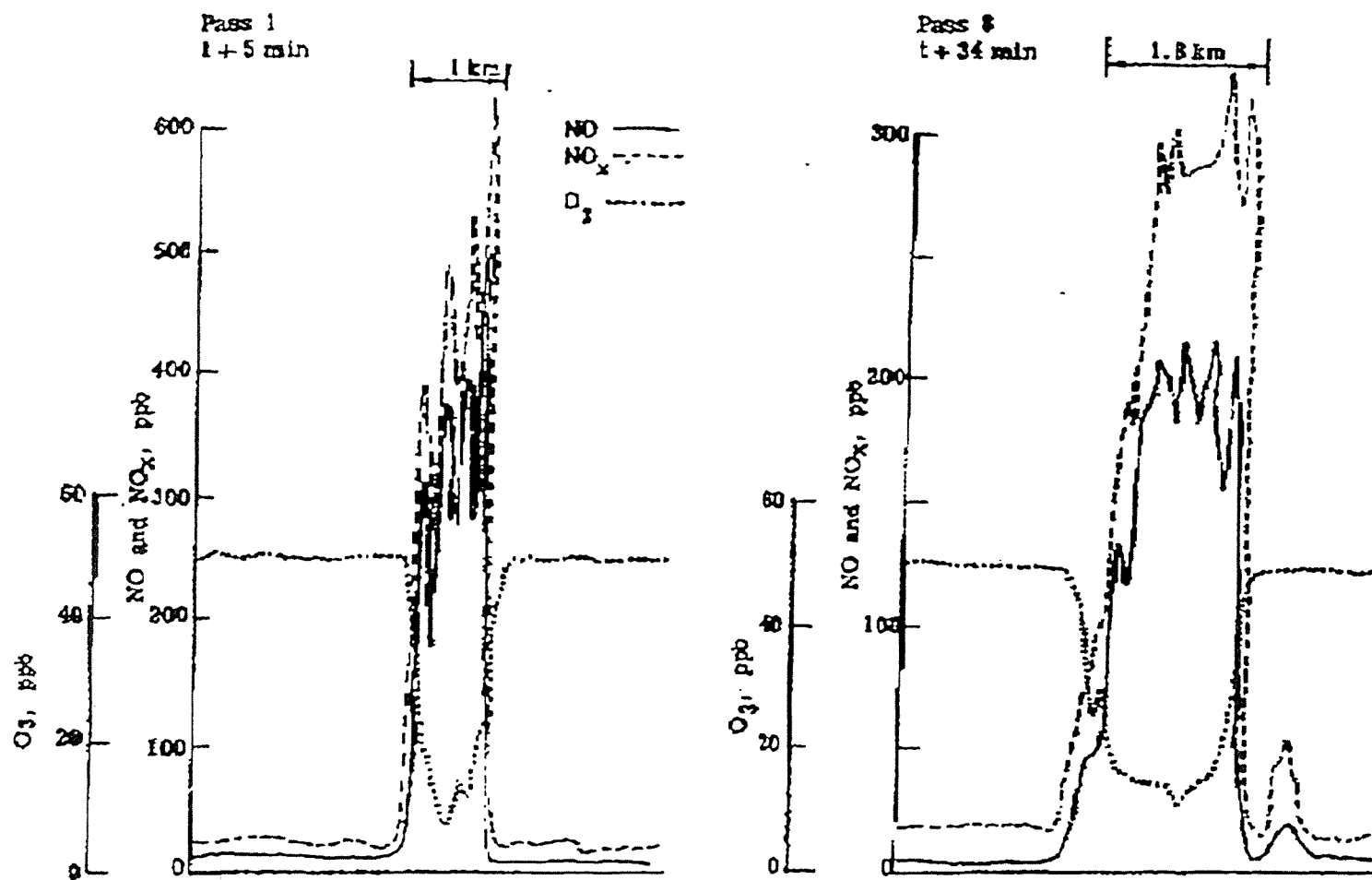


Figure 5.1. Aircraft data traces at t + 5 min and t + 34 min.

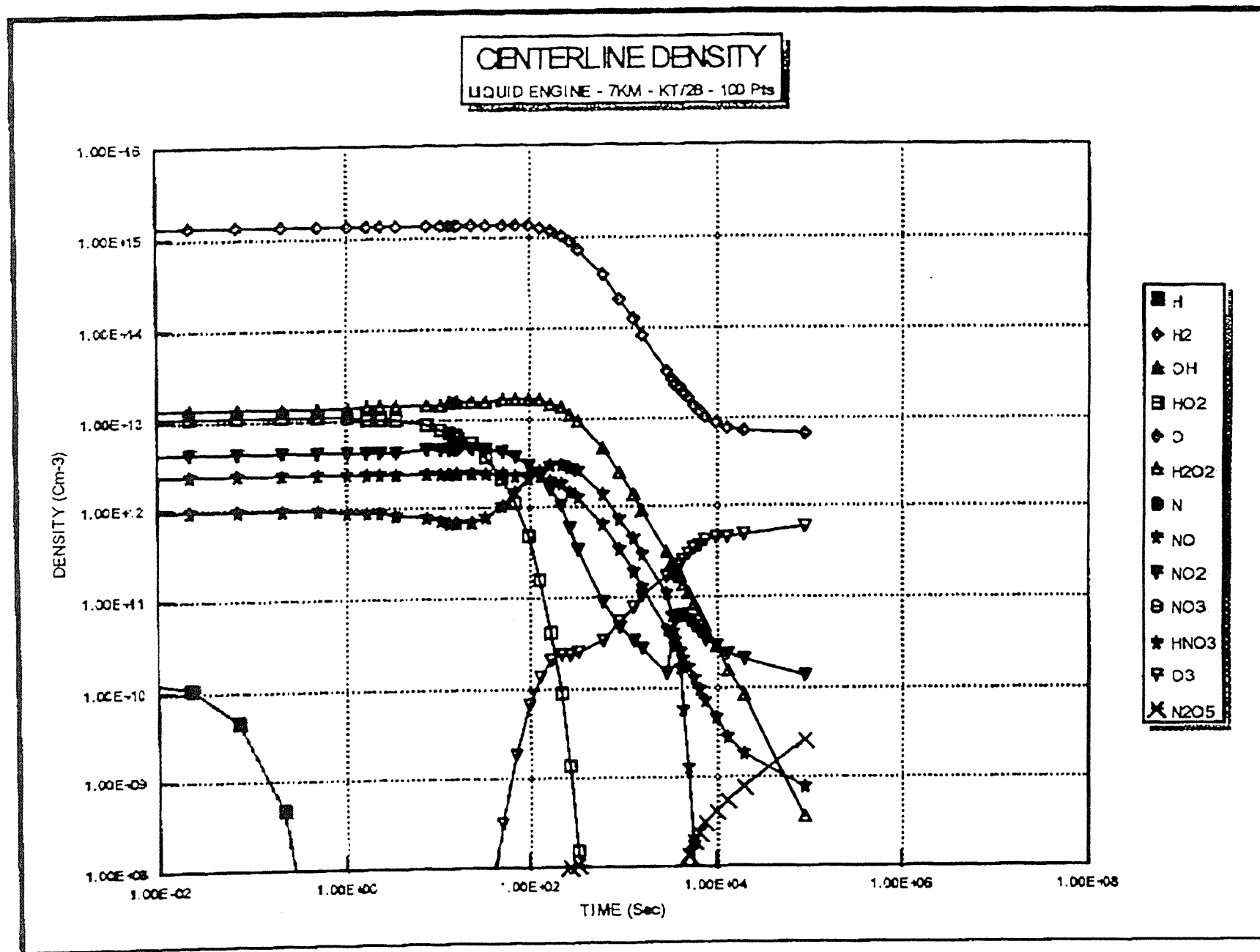


Figure 5.2. Centerline Density

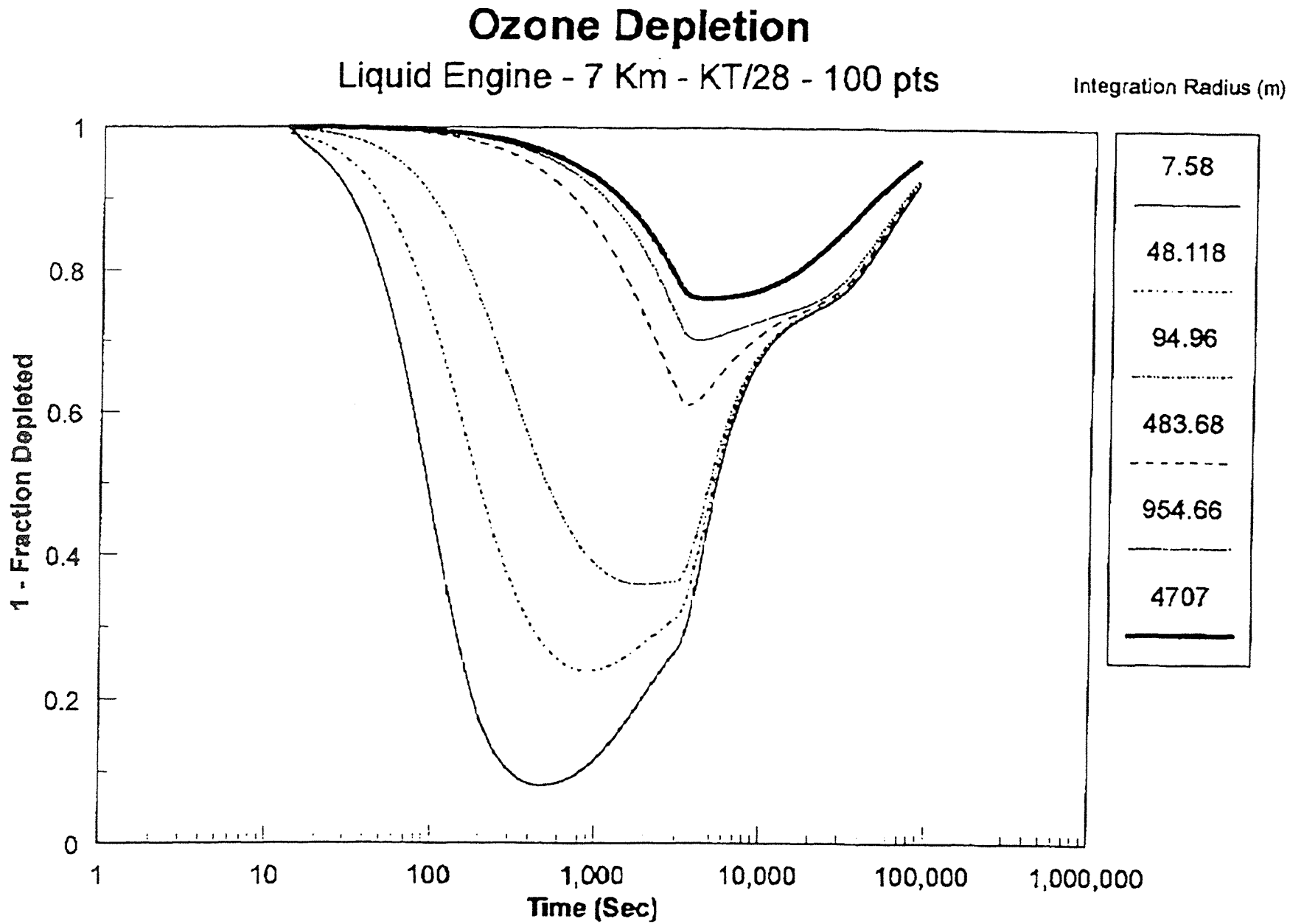


Figure 5.3. 2 Ozone Depletion

Radial Profiles at 599 sec

Liquid Engine - 7 Km - KT/28 - 100 Pts

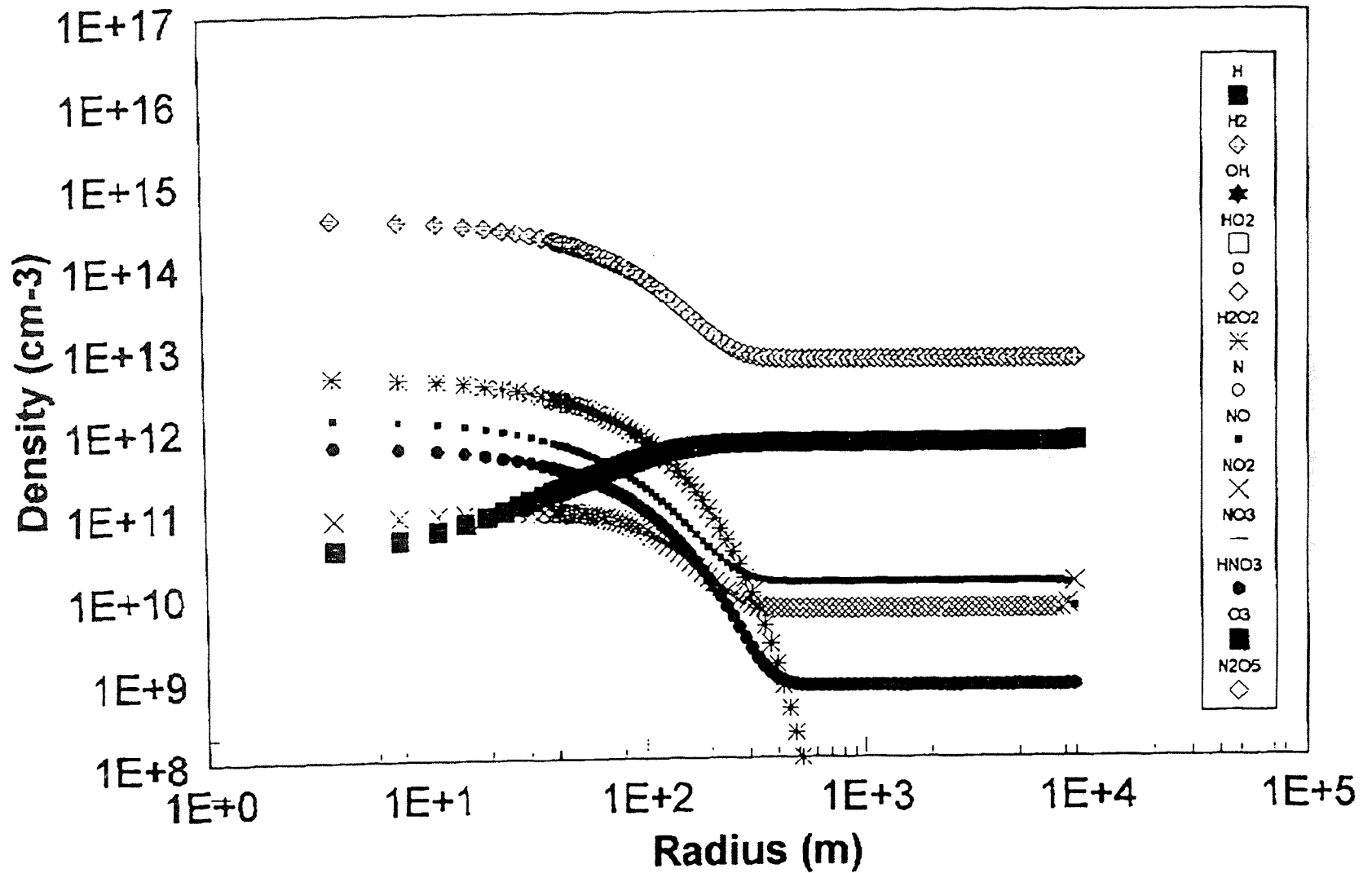


Figure 5.4. Radial Profiles at 599 sec

Radial Profiles at 5059 sec

Liquid Engine - 7 Km - KT/28 - 100 Pts

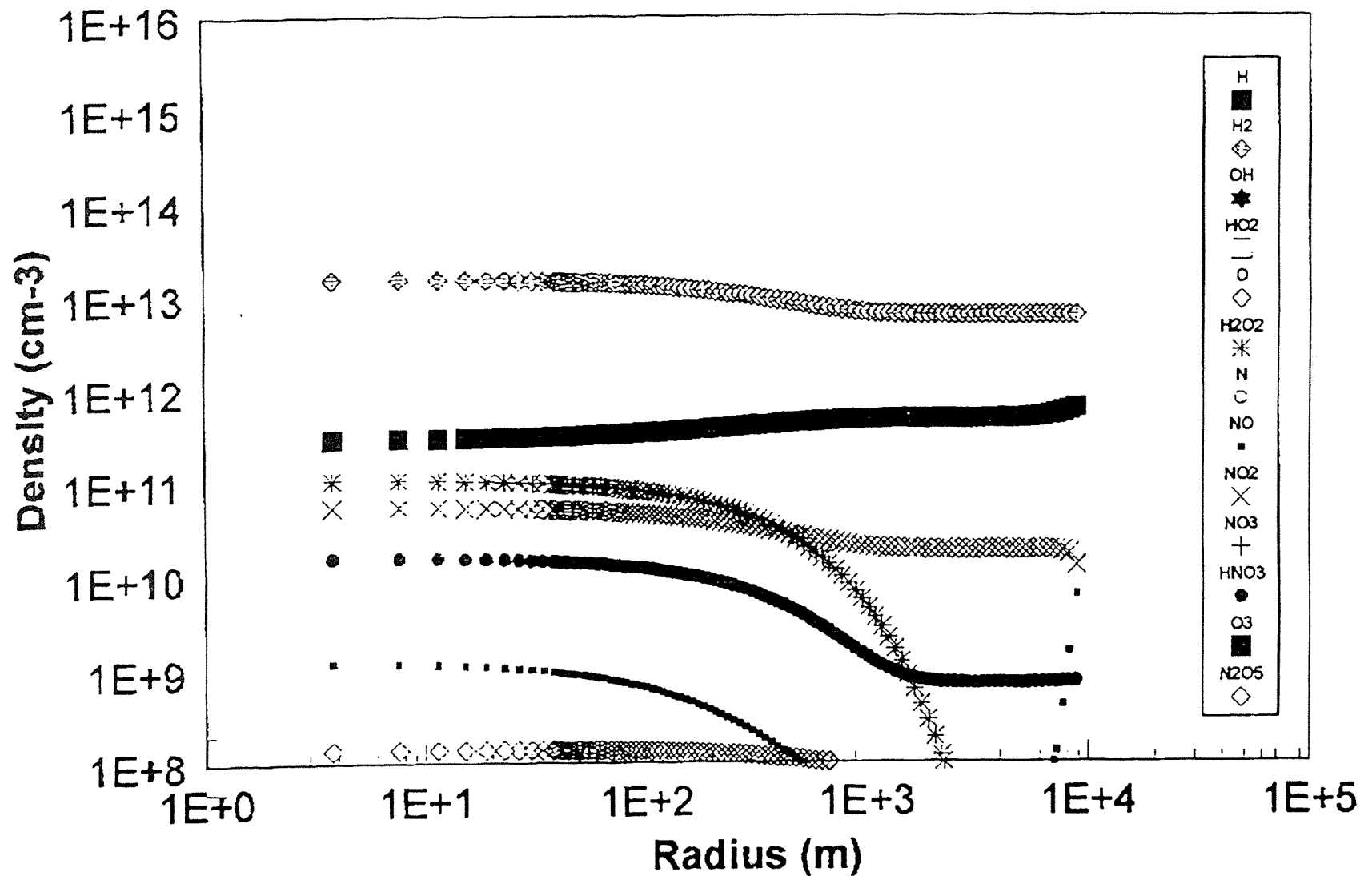


Figure 5.5. Radial Profiles at 5059 sec

5.4 ANALYSIS RESULTS

A stagnation streamline calculation was performed for a representative deorbiting debris particle. The debris particle is assumed to be a blunt-nosed body of diameter 1/2 inch, traveling at a hypersonic speed of Mach 23.0 at an altitude of 30 km. The streamline pressure distribution which is a required input for the calculation was generated from an inviscid Euler flow solution of the body and is reproduced in Figure 5.6 along with the calculated velocity and density of the one-dimensional flow. The pressure profile shows a uniform pressure distribution between the shock (at axial location =0) and the body surface, then decreases as the streamline goes around the body towards the free layer. The calculated velocity and density are seen to be consistent with that of the pressure profile, e.g., the density level drops significantly in the free layer as predicted by the hypersonic Newtonian theory. Of particular interest is the species profiles shown in Figure 5.7. In order to obtain an upper bound, initial species concentrations are assumed to be in local chemical equilibrium right behind the shock, which in the case of NO the concentration is approximately .075 in mass fraction. Additional NO is produced downstream of the flow as residence (or reaction) time increases, and a plateau is reached at about 0.1 by mass. At this mass fraction, the NO concentration is translated into 8.0×10^{15} molecule/cm³ in the near wake when bulk density of the flow is taken into account. Data obtained from the flight of the Reentry Measurements Instrumentation Package (RMIP 9) in 1969 supports the current one-dimensional analysis (Ref. 5.10). The flight involved an extensively instrumented 8° -half-angle conical reentry vehicle with a silica phenolic heatshield and a graphite tip.

Flow Properties

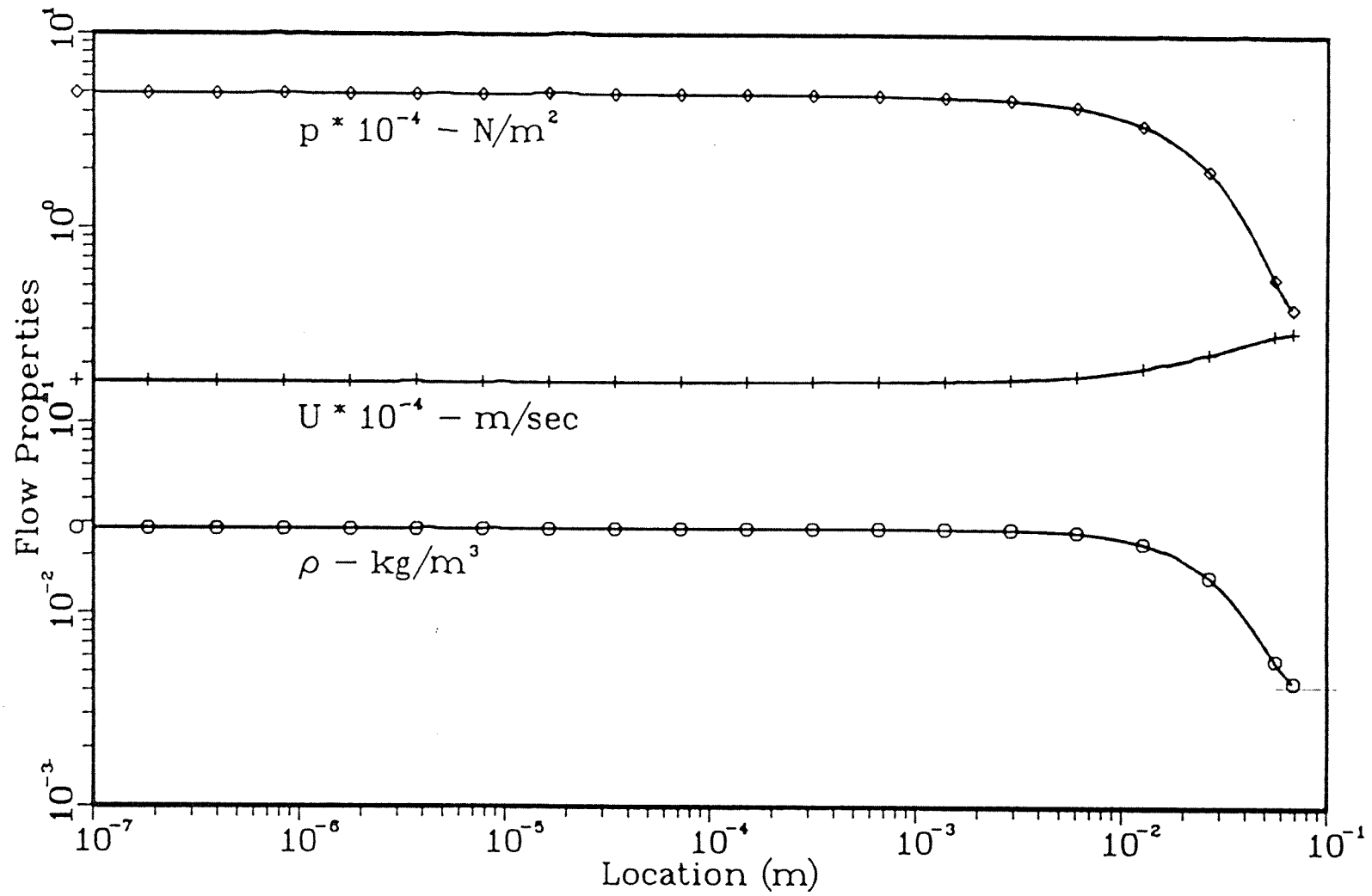


Figure 5.6.

Mass Fraction

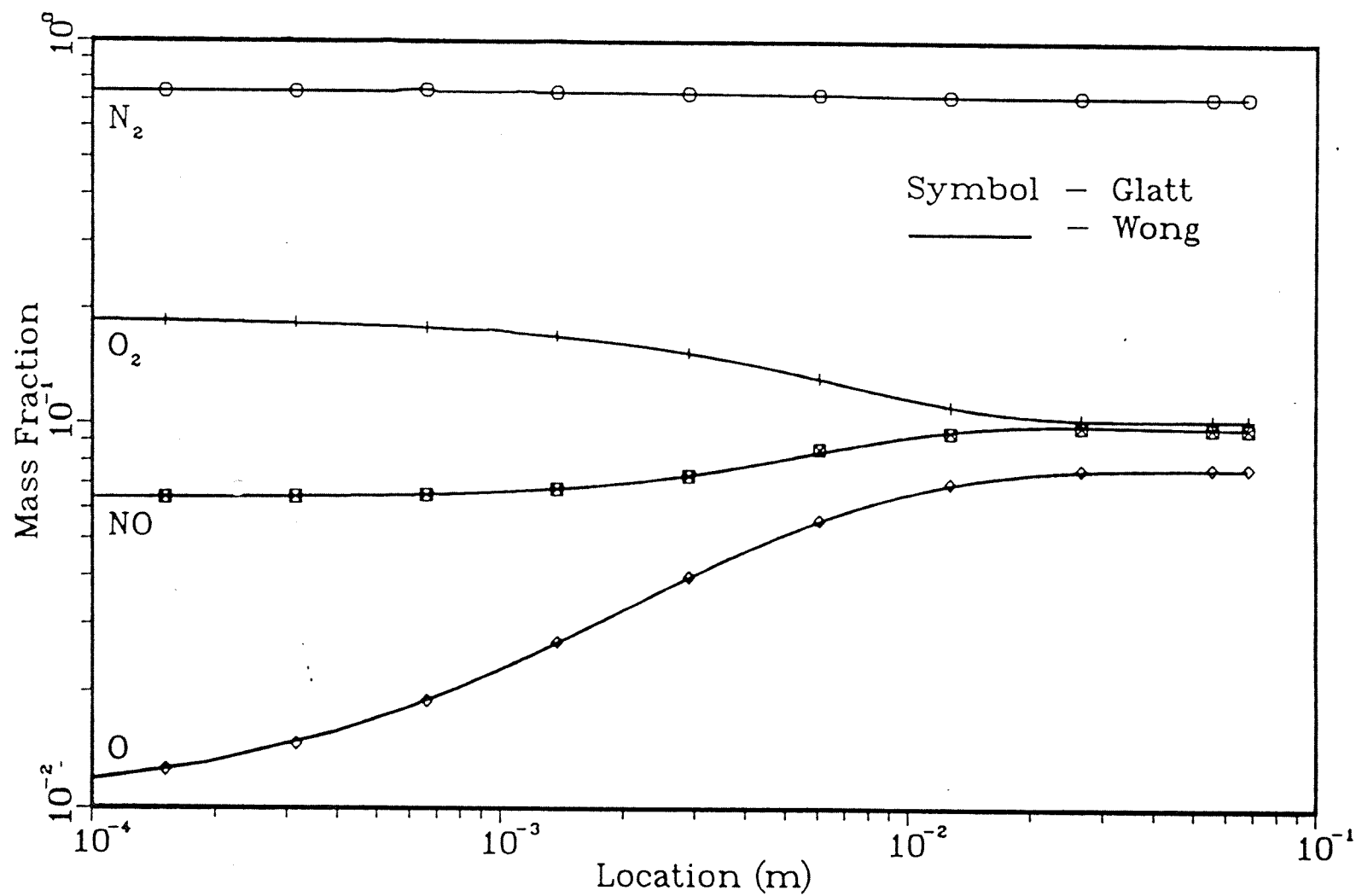


Figure 5.7.

Figure 5.8 reproduces the measured average near wake species concentration at various altitudes. Some of the species are undoubtedly generated as a result of material ablation process, but the bulk of NO is believed to be produced by the shock. According to the measurement, the NO concentration is on the order of 3×10^{15} molecule/cm³ which is essentially the same as that predicted based on the one-dimensional model.

To determine if an ozone hole is present the concentration of NO calculated for the near wake was allowed to disperse and be diluted in the far wake. The far wake analysis is based on the work of Lee & Hromas (Ref. 5.1). Taken from this paper, Figures 5.9-5.11 reproduce the enthalpy, wake width and species dispersion profiles necessary for the far wake analysis. Essentially, the enthalpy profile (Fig. 5.9) provides the downstream location (1000 x/d) at which the wake has nearly reached the ambient thermal condition. Figure 5.10 gives the wake spread of approximately 5-10 body diameters at this downstream location. If the near wake concentration of NO is assumed to be uniformly distributed in the far wake this would translate into a reduction of 10^{-2} times the concentration in the cold plume. However, Figure 5.11 can be used to provide a more accurate estimate, which at x/d=1000, the far wake dilution is between 2.6×10^{-3} and 2.0×10^{-2} depending on whether frozen or locally similar turbulence condition is assumed. By using a dilution of 2.6×10^{-3} and near wake concentration of 8.0×10^{15} molecule/cm³, the cold plume NO concentration of 2.0×10^{13} molecules/cm³ was calculated. Figures 5.12 and 5.13 show the results of the cold plume (far wake) ozone depletion calculation. Figure 5.12 shows the net rate of ozone depletion as a function of radial location with time as a parameter. At small time, 1ms, the rate of depletion

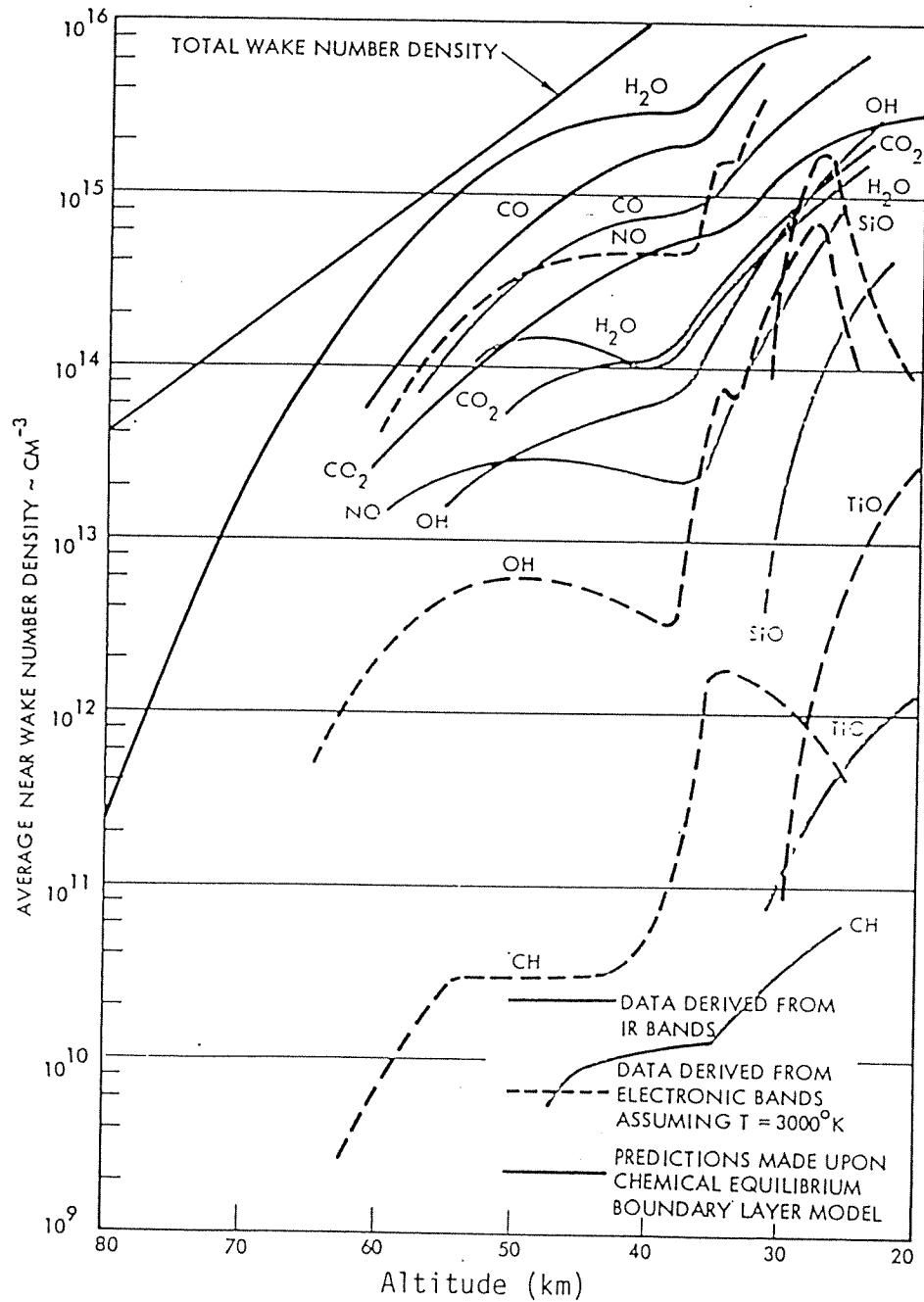


Figure 5.8.

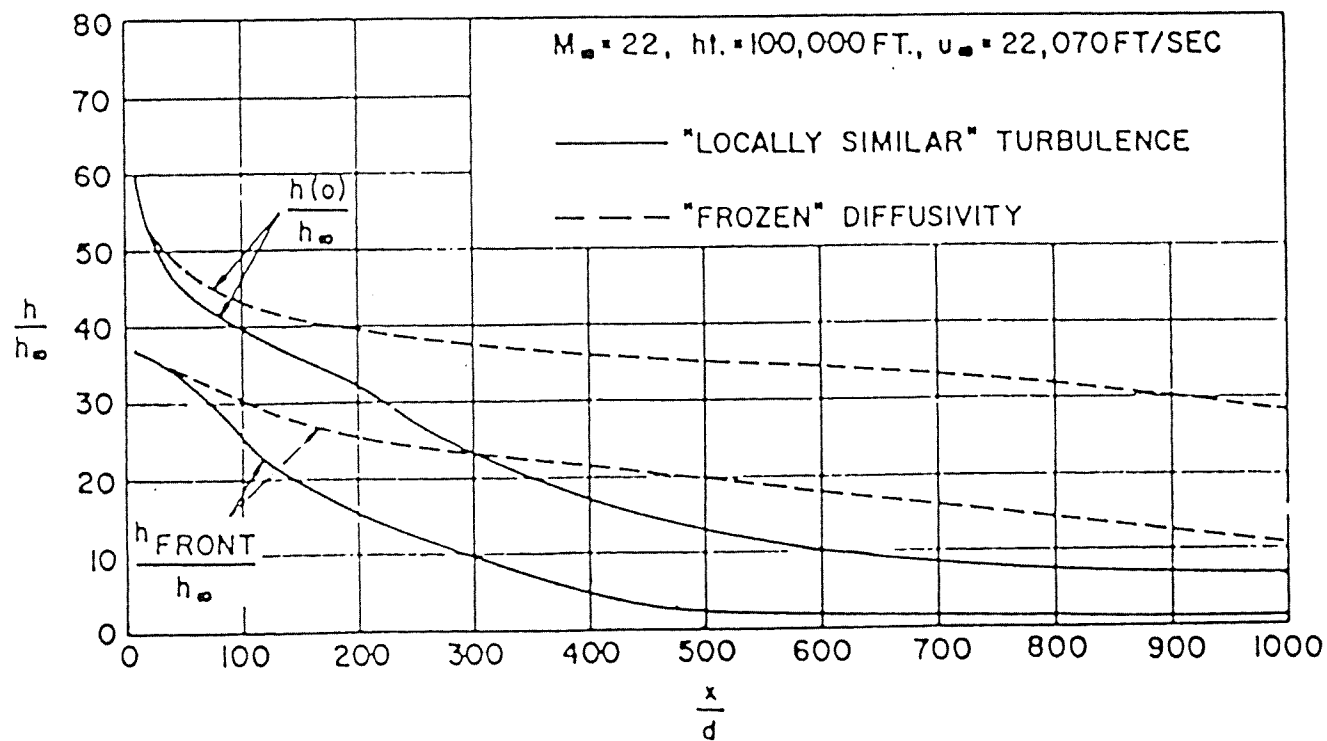


Figure 5.9. Enthalpy distribution along the axial streamline ($M_\infty = 22$ and 100,000-ft altitude).

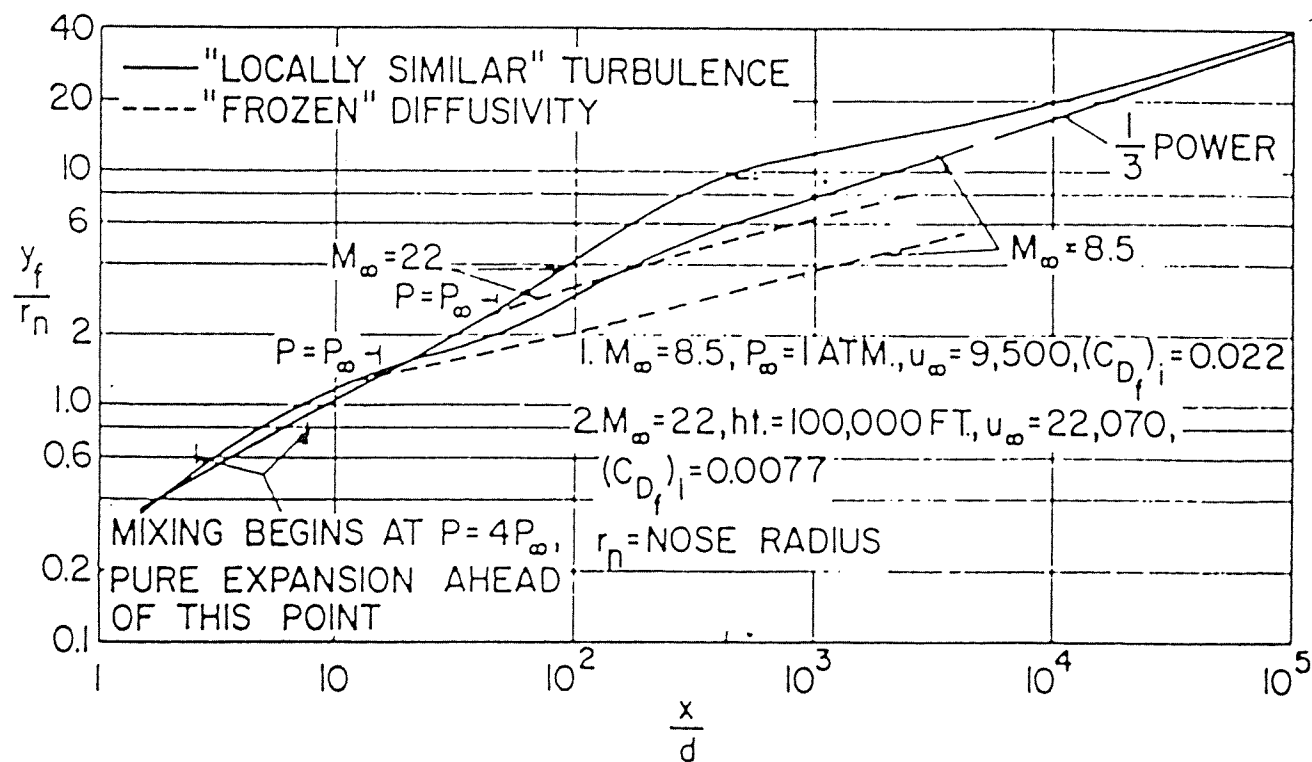


Figure 5.10. Comparison of turbulent wake width for $M_\infty = 8.5$ and $M = 22$.

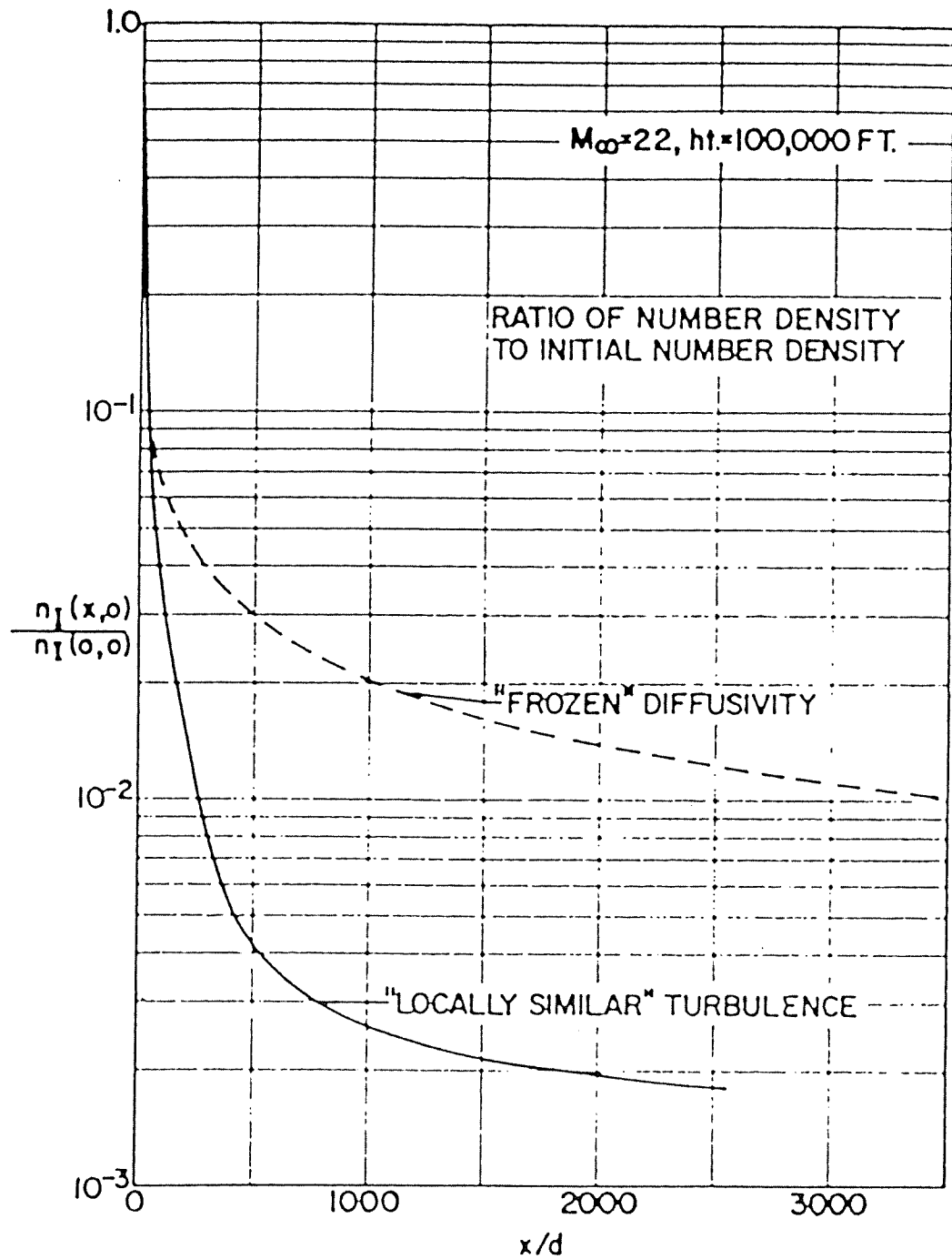


Figure 5.11. Turbulent diffusion in the wake ($M_{\infty} = 22$ and 100,000-ft altitude).

Net Rate of Ozone Loss

13 cm Wake - 30 km - NO 5E-5

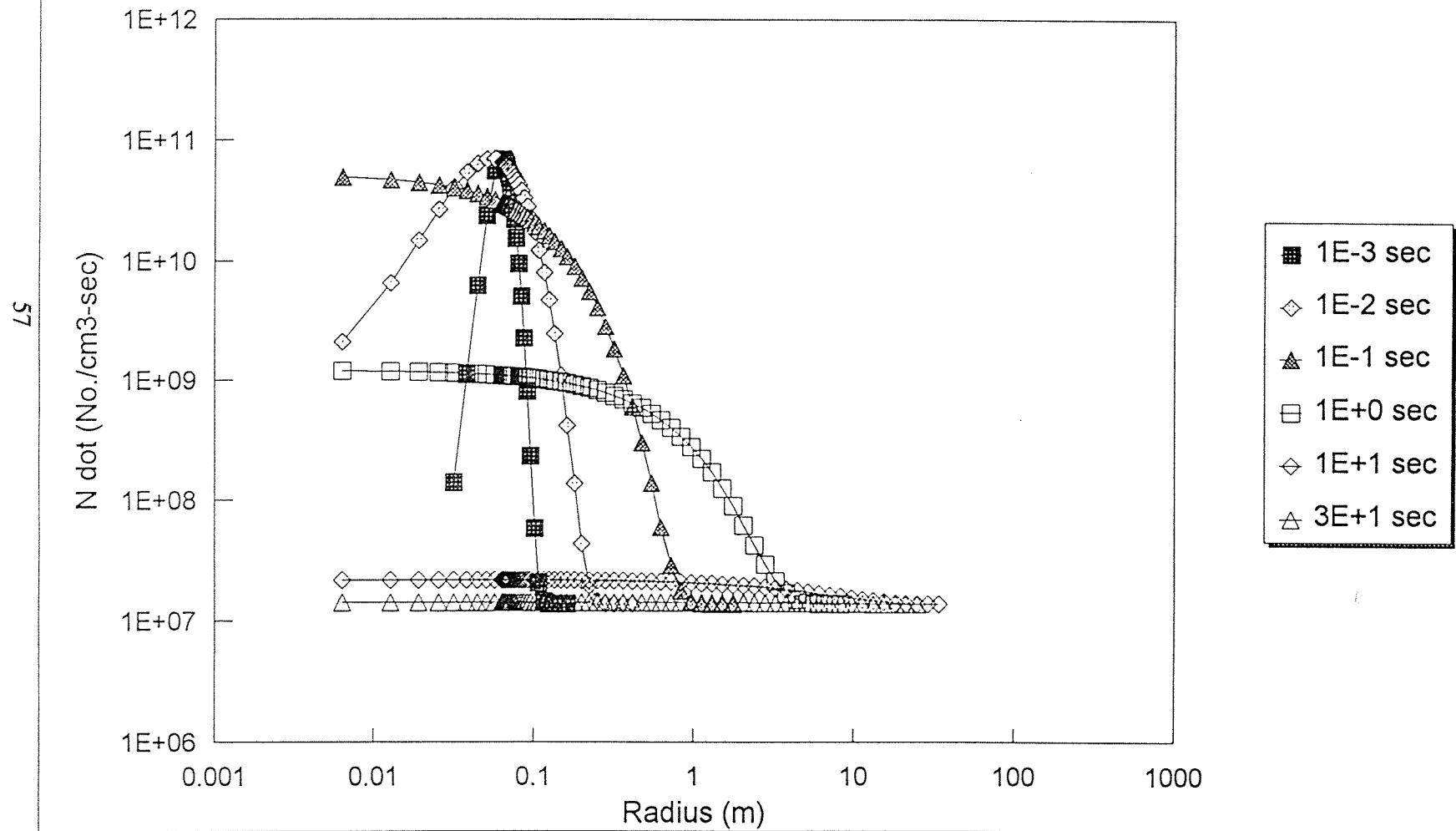


Figure 5.12.

OZONE DEPLETION

13 cm Wake - 30 km - NO 5E-5

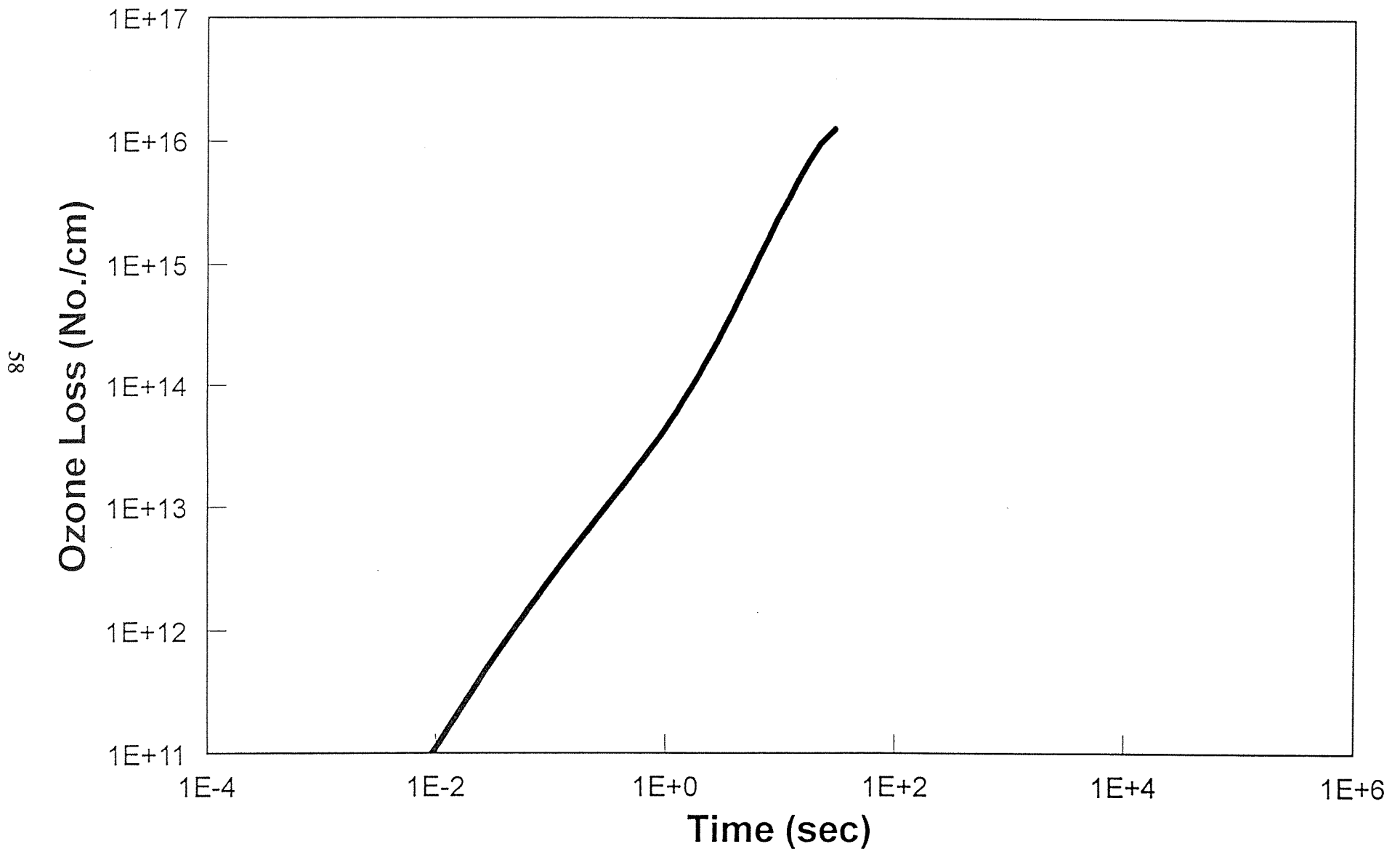


Figure 5.13.

is extremely fast due to the high concentration of NO. At larger time, 1 second, however, the rate is about two orders of magnitude lower than the initial rate indicating a rapid destruction of NO due to either chemical reaction or diffusion. At about 10 seconds, the rate has reached that of the ambient signaling the disappearance of the local hole. Clearly, the presence of an ozone hole is shown at 1 second with a radius of 1 meter. Figure 5.13 shows the cumulative ozone loss for a 1-cm cold wake. At 100 second, local depletion ozone ceases but global effect would persist because local injection still represents a source of NO.

To evaluate the global impact due to production of thermal NO behind the shock one may use the results generated from the stagnation streamline together with the deorbiting flux calculations. Figure 5.13 shows a total ozone loss due to a deorbiting debris particle of 1-cm diameter class. Based on the deorbiting reentry analysis (Section 3), particles of this class are likely to reenter the stratosphere at hypersonic speed and therefore a continuous production of thermal NO will take place as these particles pass through the atmosphere. Figure 2.1 shows the number of deorbiting debris particles reentering the stratosphere for various class of particles. Depending on the flight path angle, the varying flight-path length will deposit different amount of NO in the cold wake thus depleting ozone according to Figure 5.13.

Table 5.2 summarizes the global impact at various path angle.

TABLE 5.2 - Global Impact Due To Deorbiting Debris

Flight Path Angle, deg	Net ozone loss, molecules/year	Percent loss
20°	1.3×10^{28}	3.7×10^{-8}
40°	7.1×10^{27}	2.0×10^{-8}
60°	5.2×10^{27}	1.5×10^{-8}

According to the above simple one-dimensional streamline analysis of thermal NO production it appears that deorbiting debris of particle size larger than 1 centimeter are likely to create an ozone hole of size up to 100 diameters of the particle. The presence or the process of ozone destruction persists for up to 100 seconds. From a global standpoint, however, due to the extremely low flux of deorbiting debris (10 particles/day) the impact on stratospheric ozone is extremely small, which at the most can only account for $10^{-8}\%$ per year. In other words, the effect will not be felt for at least 10^8 years assuming that the debris flux stays relatively low.

A severely conservative upper bound can be developed for the destruction of ozone by NO produced from material bound nitrogen released during reentry. Based on the flux of debris to the stratosphere (Figure 2.3), approximately three kilograms of debris enters the stratosphere per day. We then make the (conservative) approximation that 20% of this mass is non metallic material (e.g., paints, composites) and further (conservatively) assume that 50% of the non metallic mass is converted to NO by reaction with the ambient atmosphere. We have calculated the total destruction of ozone from a cold wake with 0.1 percent NO for

four wake diameters: 1cm, 10cm, 1m, and 10m. The results are shown in Figures 5.14-5.17. The calculation accounts for the turbulent mixing and chemical reactions as the wake interacts with the ambient atmosphere. The process of ozone loss ceases when the NO concentration dilutes to the ambient background level. Examination of Figures 5.14-5.17 determines that the one meter and ten meter wakes destroy ozone in proportion to the total number of NO molecules contained while the smaller wakes are not quite as efficient. If all the NO produced per day (as conservatively estimated here as 6×10^{24} molecules) is placed into a one meter wake with $\chi_{\text{NO}}=0.001$ (a 3000m long wake), then about 3×10^{27} molecules of ozone are destroyed. There are approximately 10^{36} - 10^{37} molecules of ozone in the entire stratosphere. Hence as an upper bound, about one billionth of the stratospheric ozone (one part in 1×10^9) per day will be destroyed per day by NO produced from material-bound nitrogen.

OZONE DEPLETION

1 cm Wake - 18 km - NO $1\text{E-}3$

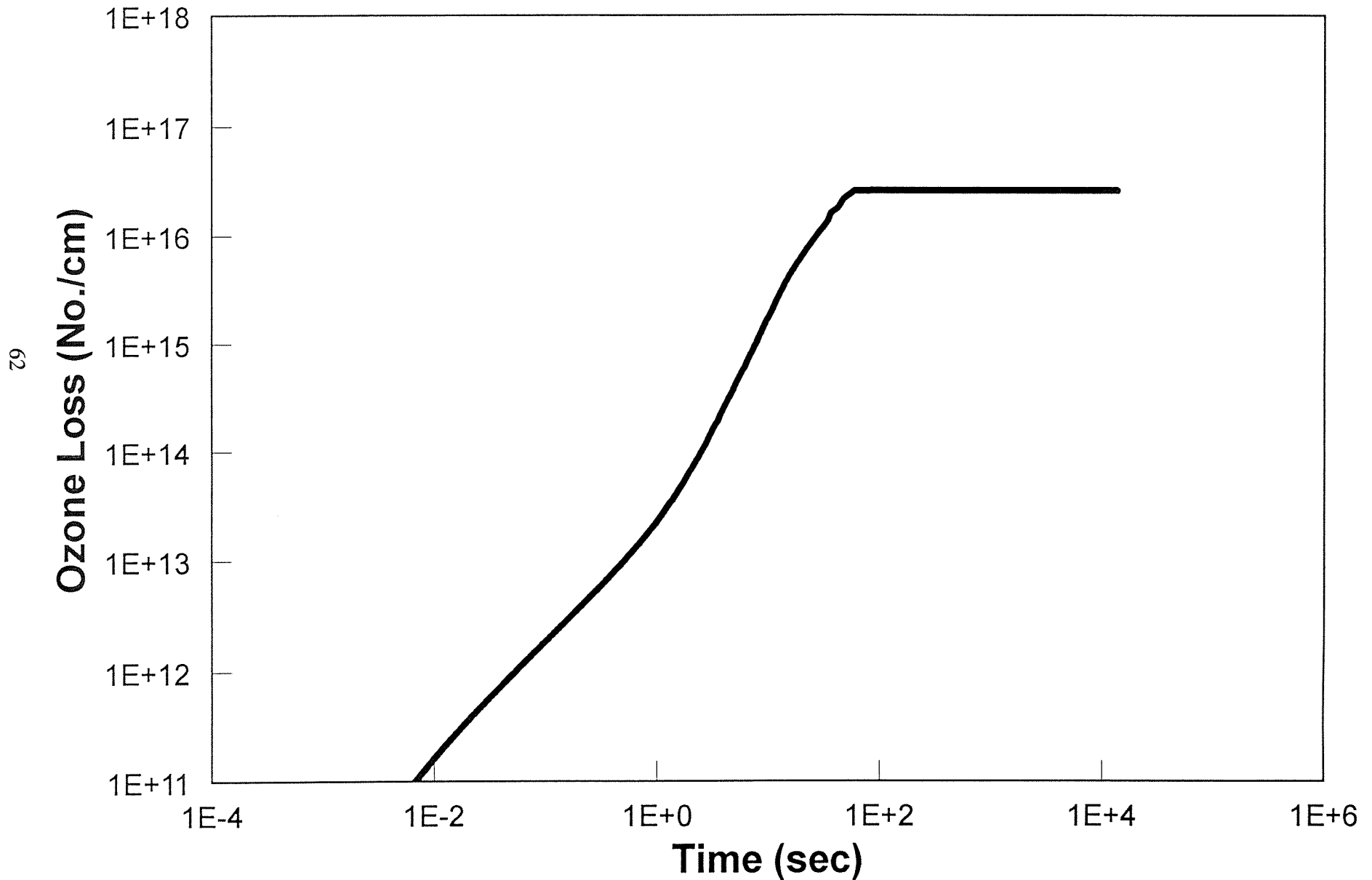


Figure 5.14.

OZONE DEPLETION

10 cm Wake - 18 km - NO 1E-3

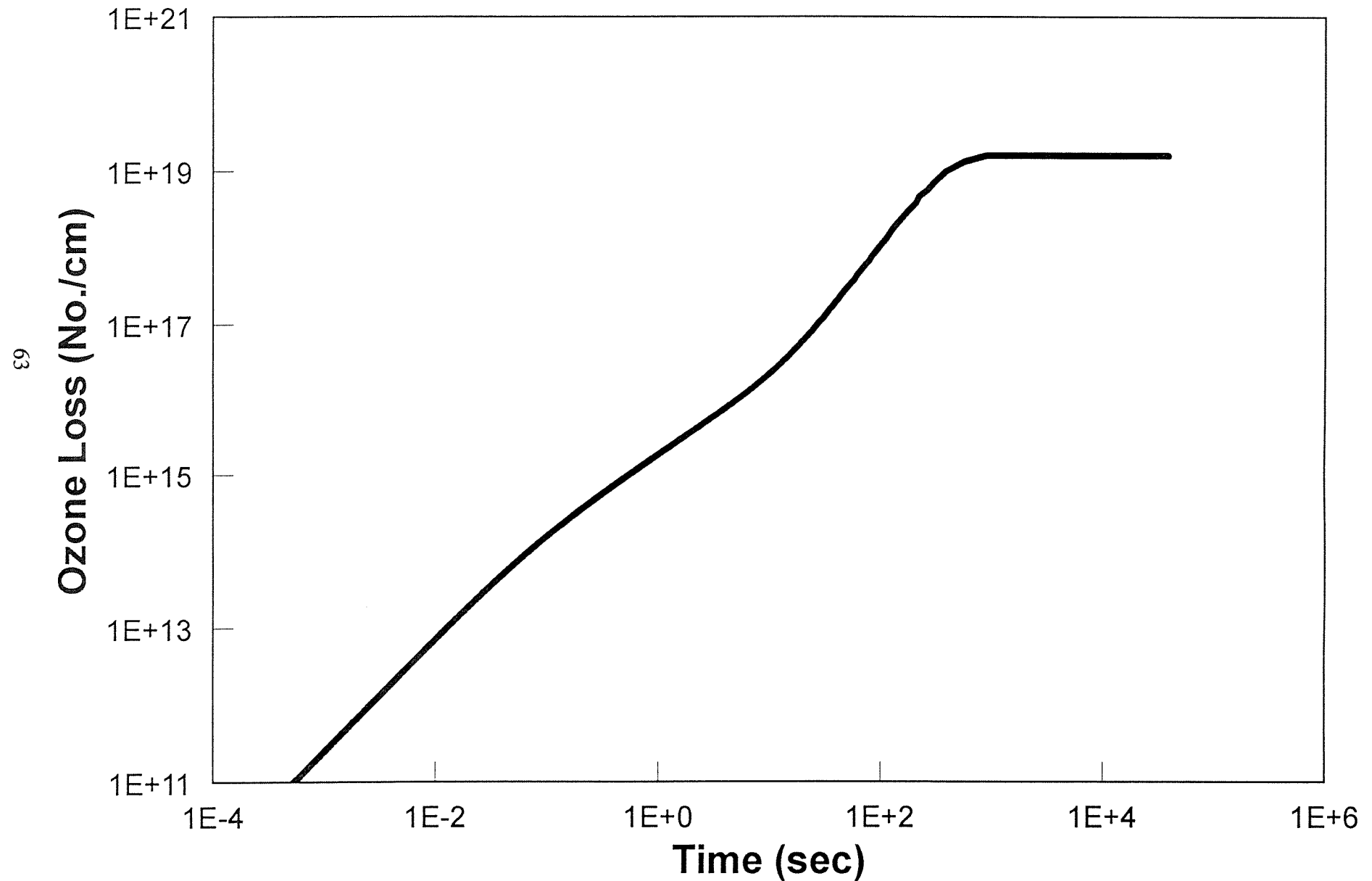


Figure 5.15.

OZONE DEPLETION

100 cm Wake - 18 km - NO 1E-3

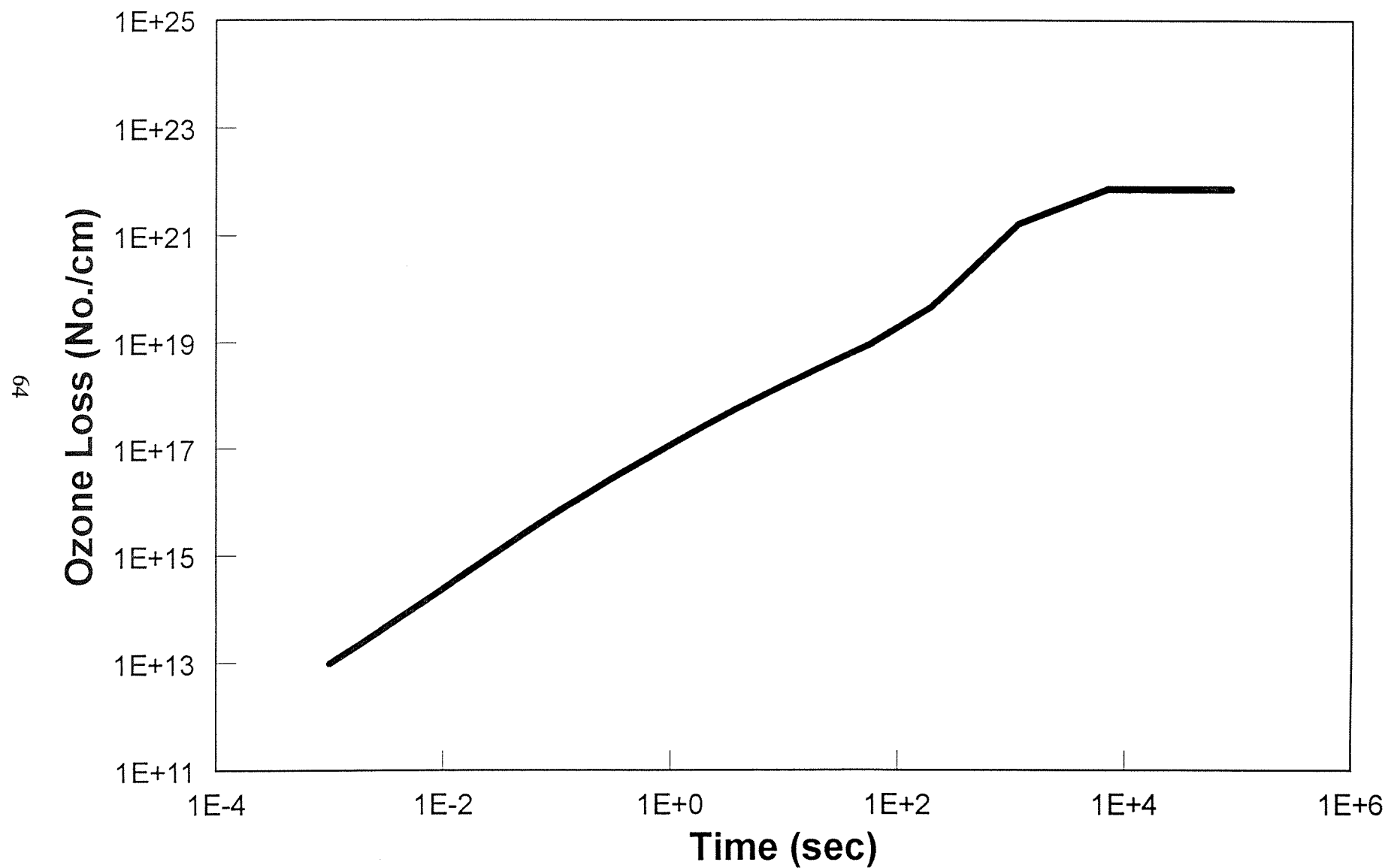


Figure 5.16.

OZONE DEPLETION

10 m Wake - 18 km - NO 1E-3

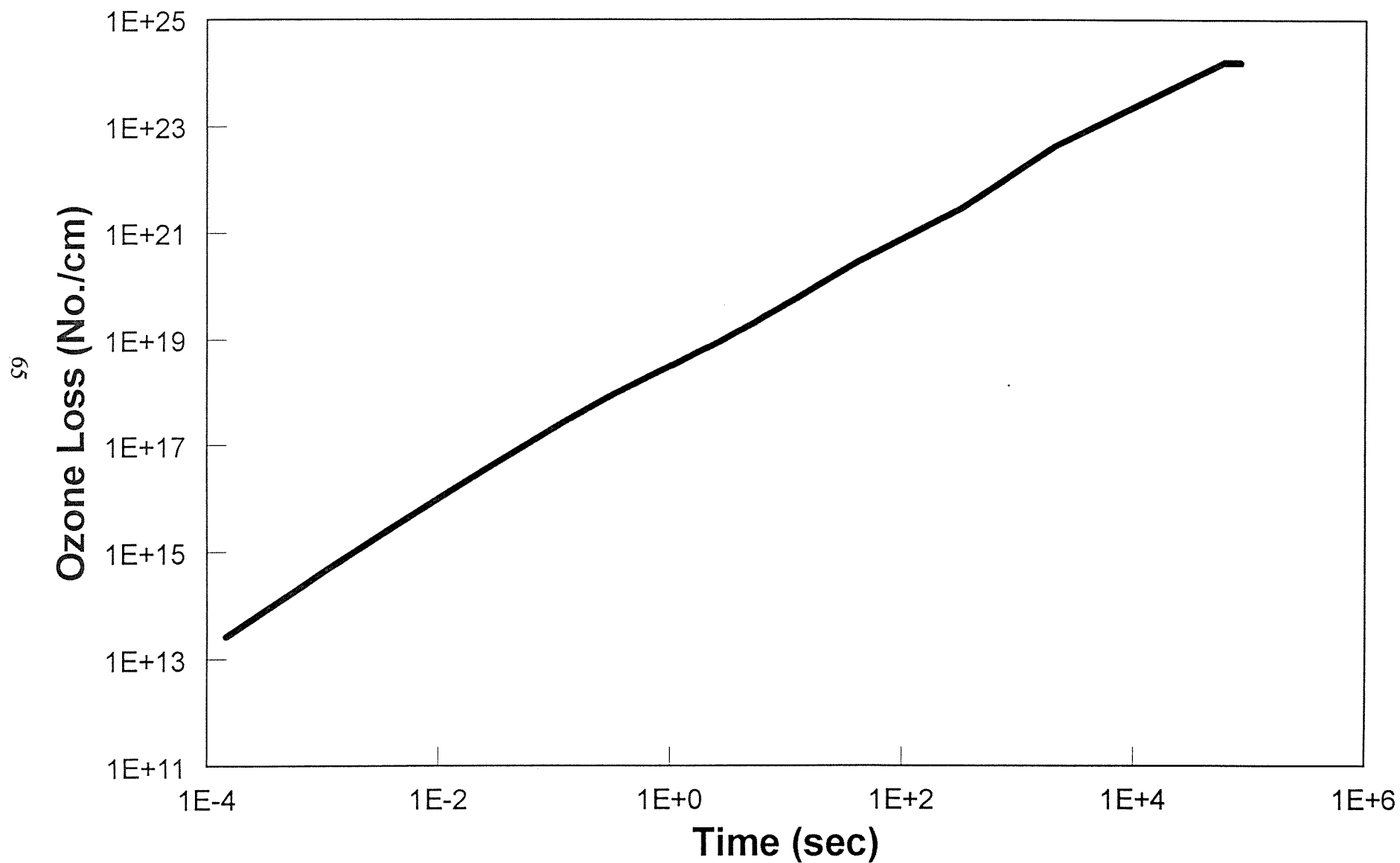


Figure 5.17.

6. Summary and conclusions

Assessment of the impact of orbital debris on stratospheric ozone requires several steps:

- 1) quantify the debris population,
- 2) quantify the orbital decay and subsequent flow of debris into the stratosphere,
- 3) assess the debris reentry/heating characteristics,
- 4) identify ozone depletion mechanisms: heterogeneous, homogeneous (with NO produced both by thermal mechanisms and by the material bound nitrogen mechanism)
- 5) quantify and/or bound ozone depletion.

The approach taken to perform these steps was to determine representative behavior, stopping short of evaluating each individual debris reentry event.

Local depletion of ozone in the stratosphere does occur. It is quantified for representative deorbiting events. The local ozone-depleted holes can be expected to occur infrequently, are relatively small, and do not persist for a very long time. Global stratospheric ozone is impacted as follows:

- 1) NO produced from material bound nitrogen is estimated, conservatively, to destroy one part in one billion stratospheric ozone molecules per day;
- 2) NO produced by thermal mechanisms behind the debris bow shock is estimated to destroy one part in 10 billion stratospheric ozone molecules per year,

3) Destruction of one percent stratospheric ozone by heterogeneous mechanisms is estimated to require 3×10^5 years.

Examination of Ref. 2.3 shows that the meteoroid population for micron-millimeter size objects is comparable to the orbital debris flux. To the extent that they are comparable, one concludes that meteoroids pose little or no threat to global stratospheric ozone.

Consideration of the above results lead to the conclusion that the physical and chemical phenomena associated with deorbiting debris (and possibly meteoroids) do not have a significant impact on global stratospheric ozone. It is also noted that large particle deposition from heavy, large thrust, rocket launches may create an environment where a large amount of local O_3 may be depleted.

References

1.1 "Solid Rocket Exhaust in the Stratosphere: Plume Diffusion and Chemical Reactions", M. R. Denison, J. L. Lamb, W. D. Bjorndahl, E. Y. Wong, P. D. Lohn; to be published in the Journal of Spacecraft & Rockets, July-August 1994.

2.1 AIAA-016-1922, Orbital Debris Mitigation Techniques: Technical, Legal, and Economic Aspects, 1992.

2.2 "The risk of collision between manned space vehicles and orbital debris-Analysis and basic conclusions," P. Eichler and D. Rex, Z. Flugwiss. Weltraumforsch (ZFW) 14(1990) pages 145-154, Springer Verlag 1990.

2.3 NASA SSP 30425, Revision A, June 1991.

2.4 Personal communication with P. D. Anz-Meador.

2.5 "Shuttle/Spacelab Contamination Environment and Effects Handbook," L. E. Bareiss, R. M. Payton, H. A. Papazian, NASA Contractor Report 4053, 1987.

2.6 Personal communication with F. D. Cottrell.

- 3.1 Molecular Gas Dynamics, G. A. Bird, Oxford Press, 1976.
- 3.2 "Analytical Methods Used in Predicting the Re-Entry Ablation of Spherical and Cylindrical Bodies," O. Cropp, Sandia Report SC-RR-65-187, 1965.
- 3.3 Hypersonic Flow Theory, W. D. Hayes & R. F. Probstein, Academic Press, 1959.
- 3.4 "Hypersonic Aerodynamics," Course Note 9, R. H. Korkegi, Von Karmen Institute for Fluid Dynamics, Rhode-Saint-Genese, Belgium, June 1961.
- 3.5 "Theory of Stagnation Point Heat Transfer in Dissociated Air," J. A. Fay & F. R. Riddell, Journal of the Aeronautical Sciences, v25,n2, February, 1958.
- 3.6 "Stagnation Point Heat-Transfer Measurements in Dissociated Air," P. H. Rose & W. I. Stark, Journal of the Aeronautical Sciences, v25, n2, February, 1958.
- 3.7 "Review of Orbital Reentry Risk Predictions," O. Refling, R. Stern, C. Potz, Aerospace Report No. ATR-92(2835)-1, July, 1992.
- 3.8 "Space Debris Reentry Risk Analysis," S. A. Bouslog, B. P. Ross and, C. B. Madden, AIAA paper 94-0591, presented at AIAA 32nd Aerospace Sciences Meeting, January 1994.
- 4.1 J. C. Farman, B. G. Gardiner, J. D. Shanklin, Nature, v315, 1985.

4.2 M. J. Molina, R. Zhang, P. J. Woodbridge, J. R. McMahon, J. E. Kim, H. Y. Chang, K. D. Beyer, Science, v261, September 1993.

4.3 S. J. Solomon, R. R. Garcia, F. S. Rowland, D. J. Wuebbles, Nature, v231, June 1986.

4.4 "Stratospheric Chemistry of Aluminum Oxide Particles," R. Meads, D. D. Spenser and M. J. Molina, Report to TRW, June 1994 (included as Appendix 1 in the present report).

4.5 J. P. D. Abbat & M. J. Molina, J. Phys. Chem., v96, n19, 1992

4.6 W. E. Ranz, & W. R. Marshall, Chem. Eng. Prog., v48, 1952.

4.7 M. E. Zolensky, D. S. McKay, L. A. Kaczor, J. Geophys. Res, v94, nD1, 1989.

4.8 "Eruptions of the St. Augustine volcano: airborne measurements and observations," P. V. Hobbs, L. F. Radke, and J. L. Stith, Science, v195, 1977.

5.1 "Turbulent Diffusion in the Wake of a Blunt-Nosed Body at Hypersonic Speeds," L. Lees & L. A. Hromas, J. Aerospace Sciences, v29, 1962.

5.2 "Measured Properties of the Wakes of Hypersonic Cones," J. Herrman, R. E. Slattery, and W. G. Clay, AIAA paper 68-687, presented at AIAA Fluid and Plasmadynamics Conference, 1968.

- 5.3 "Transition Correlations for Hypersonic Wakes," S. Zeiberg, AIAA, v2, n3, 1964.
- 5.4 "The Far Wake behind Cylinders at Hypersonic Speeds. Part I: Flowfield," H. W. Behrens, AIAA, v5, n12, 1967.
- 5.5 Personal discussions with H. W. Behrens & R. G. Batt, 1994.
- 5.6 "A Theory of Upper-Atmosphere Ozone," S. Chapman, Q.J.R. Meteorol. Soc. v3, 1930.
- 5.7 "The Production of Nitric Oxide in the Troposphere as a Result of Solid-Rocket-Motor Afterburning," R. B. Stewart & R. I. Gombert, NASA TN D-8137, 1976.
- 5.8 "Temporal Changes in the Horizontal Diffusion Parameter of a Single Nuclear Debris Cloud," D. Randerson, J. Appl. Meteor. v11, 1972.
- 5.9 "Chemical Kinetics and Photochemical Data for Use in Stratospheric Modeling," NASA Panel for Data Evaluation (number 9), JPL Publication 90-1, 1990.
- 5.9 Chemistry of the Natural Atmosphere, P. Warneck, Academic Press, 1988.
- 5.10 "Analysis of RMIP 9 Optical Reentry Data I: Silica Phenolic Ablation and Flowfield Chemistry," TRW 06488-6520-R300, U. S. Army Con No DAH-C60_69_C0008.

Appendix

This appendix contains the final report from Professor Mario Molina at the Massachusetts Institute of Technology on the Stratospheric Chemistry of Aluminum Oxide Particles.

Stratospheric Chemistry of Aluminum Oxide Particles

Roger Meads, Darryl D. Spencer, and Mario J. Molina

Department of Earth, Atmospheric and Planetary Sciences

and Department of Chemistry

Massachusetts Institute of Technology

June 1994

Report

to

TRW Space and Technology Group

One Space Park Drive

Redondo Beach, CA 90278

Attn. Dr. John J. Lamb

Introduction

The emissions from solid rocket motors (SRMs) include hydrogen chloride vapor (HCl) and other inorganic chlorine compounds, as well as aluminum oxide particles. The effects of these emissions on stratospheric ozone have been investigated by Prather et al. [1], Pyle [2], and others. Recent satellite observations show no measurable localized depletion of ozone following a Space Shuttle launch [3]; nevertheless, it is possible for the effects to be quite pronounced in the immediate neighborhood of the rocket plume.

The stratospheric effects of SRM emissions on a global scale might also be of importance. If the altitude of injection is taken into account, the consequences for ozone depletion of chlorine released by SRMs are expected to be practically the same -on an atom per atom basis- as those of chlorine released by the decomposition of CFCs. The reason is that the various inorganic forms of chlorine interconvert to each other on a time scale which is short compared to the residence time of these species in the stratosphere, which is measured in years. A separate effect on stratospheric ozone from SRM emissions is that resulting from the surface chemistry promoted by alumina particles, which could lead to enhanced ozone depletion through catalytic chlorine activation; such an effect is potentially more important than that resulting from the direct chlorine injection. Surface reactions leading to chlorine activation are well documented for stratospheric aerosols at high latitudes, i.e. low temperatures; such heterogeneous reactions play a key role in polar ozone depletion (see e.g., our recent reviews of the stratospheric ozone problem [4,5]). At low latitudes these aerosols consist predominantly of rather concentrated sulfuric acid solutions (> 50 % weight), which are inefficient for chlorine activation because of the very low solubility of HCl in such solutions. On the other hand, alumina particles can in principle promote

chlorine activation catalytically even at low latitudes. In order to assess this possibility, we have carried out laboratory investigations on the chlorine activation efficiency of alumina surfaces; the results are presented in this report.

Cofer and Pellett [6] carried out investigations of the interaction of HCl and H₂O on various types of aluminum oxide surfaces, showing that chemisorption as well as physical adsorption takes place. However, their experiments were not carried out at low temperatures, and more importantly, the H₂O and HCl partial pressures employed were orders of magnitude above those applicable to the stratosphere. Furthermore, little if anything can be inferred from such experiments in terms of the efficiency for chlorine activation in the stratosphere by the surfaces in question.

Reactivity of ClONO₂ + HCl On α -Alumina Surfaces

We have carried out measurements of the reaction probability of ClONO₂ + HCl on α -Alumina surfaces under typical stratospheric conditions of temperature and reactant partial pressures. The experiments were performed in a low pressure - fast flow reactor, operated at steady state, fitted with a movable injector, and coupled to a quadrupole mass spectrometer. This technique is similar to that used previously by our group to measure the reaction probabilities of processes such as ClONO₂ + HCl and HOCl + HCl on ice, NAT and SAT [7,8,9]. The experimental procedure consisted of measuring the reactant ClONO₂ decay and product Cl₂ appearance at steady state in the presence of excess HCl vapor as a function of injector position, and from these we determined the respective pseudo first order rate coefficients. Experiments were conducted in dry Helium buffer gas or Helium humidified with $3\text{--}5 \times 10^{-4}$ torr of water at total pressures near 1 torr; there were no significant differences in the reaction rates with water vapor added. The partial pressures of ClONO₂ and HCl were in the range

of 10^{-7} to 10^{-6} torr, which correspond to typical lower stratospheric values. The measured first order rate coefficients, determined by a non-linear least squares fitting routine, were corrected for the effects of radial diffusion [10].

The α -alumina samples employed in our experiments were obtained from Aldrich Chemical Company; they consisted of < 3 mm diameter sintered pieces (with irregular shapes). Although the surface area of these alumina particles was not accurately known, it could be estimated by geometric considerations assuming a non-porous surface. On the other hand, since the detailed flow dynamics -and hence, the surface collision frequency- is difficult to model accurately for the system containing the alumina particles, the reaction probability was determined by comparison to that measured on glass pieces of comparable dimensions. The alumina or glass particles were placed in a Teflon boat, and the walls of the glass flow-tube reactor were covered with a Teflon sleeve which we determined to have a reaction probability at least two orders of magnitude smaller than that of glass. The reaction probability on a glass surface was measured directly in separate experiments using a cylindrical glass tube, for which the flow dynamics is well understood.

Typical measured reactant decays and product buildups are shown in figure 1 to 3; the injector position has been converted to time, taking into account the gas flow velocity. Calculated reaction probabilities are shown in table 1. The reaction probabilities exhibited no measurable temperature dependence over the range -20 to -75 °C.

Control experiments were carried out to measure the reaction probabilities on ice and on 60 wt. % H_2SO_4 surfaces to confirm that we were able to measure the much higher reaction probability on ice -greater than 0.1- and the essentially non-reactivity

on 60 wt. % H_2SO_4 . The results we obtained in these experiments were in good agreement with accepted values. Our measurements yield a reaction probability of $\text{ClONO}_2 + \text{HCl}$ on α -alumina surfaces of 0.01 - 0.02.

Seeding Experiments

Besides chlorine activation, the alumina particles emitted by SRMs have the potential to function as nucleation centers for the formation of polar stratospheric clouds. The more prevalent type I cloud particles are believed to consist of nitric acid trihydrate (NAT). We investigated in the laboratory the ability of alumina particles to nucleate NAT from supercooled nitric acid solutions (3:1 $\text{H}_2\text{O}:\text{HNO}_3$). We found the alumina not to be a good seed for the nucleation of NAT. The control experiment consisted of using NAT crystals as seeds; as expected, these did induce the rapid nucleation of the entire supercooled solution.

Stratospheric Implications

The measured reaction probability of $\text{ClONO}_2 + \text{HCl}$ on α -alumina is an order of magnitude less than that on ice and water-rich NAT surfaces. The role of surfaces such as alumina in the activation of chlorine at polar latitudes is expected to be small and their effect limited, even if the reaction probability were to be above 0.1, given their small abundance relative to polar stratospheric clouds. However, at mid-latitudes, characterized by higher temperatures where ice and NAT do not form, they could have a more significant role in chlorine activation and subsequent ozone depletion. Our results indicate that other related particles such as those of meteoritic origin may also play a role in the depletion of ozone at mid-latitudes.

The background aerosol particles prevalent at low latitudes consist of liquid sulfuric acid solutions with concentrations in the range from about 50 to 70% by weight H_2SO_4 . Chlorine activation on these liquid aerosols occurs extremely inefficiently as a consequence of the very small solubility of HCl on these concentrated solutions. Hence, even if alumina particles represent only a small fraction of the total aerosol loading, they have the potential to affect, at mid-latitudes, the partitioning of chlorine between active and inactive forms.

In summary, the ozone depletion potential of SRMs could be significantly larger than that estimated on the basis of chlorine emissions alone, if the catalytic efficiency for chlorine activation by alumina particles is taken into account.

References

- [1] M.J. Prather, M.M. Garcia, A.R. Douglass, C.H. Jackman, M.K.W Ko, and N.D. Sze, *J. Geophys. Res.*, **95** (1990) p. 18,583

- [2] J.A. Pyle, Report on the predicted effects of Ariane-V on the atmosphere using a two-dimensional model, submitted to ESA, 1991.

- [3] R.M. McPeters, M. Prather and S. Doiron, *J. Geophys. Res.*, **96** (1991) p. 17,379

- [4] J.P.D. Abbatt and M.J. Molina, *Annual Review of Energy & Environment*, **18** (1993) p.1

- [5] T.L. Shen, P.J. Wooldridge and M.J. Molina, Stratospheric Pollution and Ozone Depletion, in *Composition, Chemistry and Climate of the Atmosphere*, edited by H.B. Singh, Van Nostrand Reinhold, (1994), in press.

- [6] W.R. Cofer and G.L. Pellett, NASA Technical Paper 1105 (1978)

- [7] J.P.D Abbatt and M.J. Molina, *Geophys. Res. Lett.* **19** (1992) p. 461

- [8] J.P.D. Abbat and MJ Molina, *J. Phys. Chem.* **96** (1992) p. 7674

- [9] R. Zhang, J.T. Jayne, and M.J. Molina, *J. Phys. Chem.* **98** (1994) p. 867

- [10] R.L. Brown, *J. Res. Nat. Bur. Stan.* **83** (1978) p. 1

Table 1. Average results from experiments¹.

	Glass Tube	Glass Beads	α -Alumina
$\langle k_{\text{obs}} \rangle$	$177 \pm 18 \text{ sec}^{-1}$	$153 \pm 10 \text{ sec}^{-1}$	$138 \pm 11 \text{ sec}^{-1}$
$\langle \gamma_{\text{measured}} \rangle$	$.022 \pm .005$	$.017 \pm .002$	$.014 \pm .002$

$$\gamma_{\alpha\text{-alumina}} = \gamma_{\text{glass}} \cdot \frac{\gamma_{\alpha\text{-alumina measured.}}}{\gamma_{\text{glass beads. measured.}}} = .019 \pm .005$$

¹ Results are an average of 10 points each.

ClONO₂ + HCl on Glass Tube at -60 °C

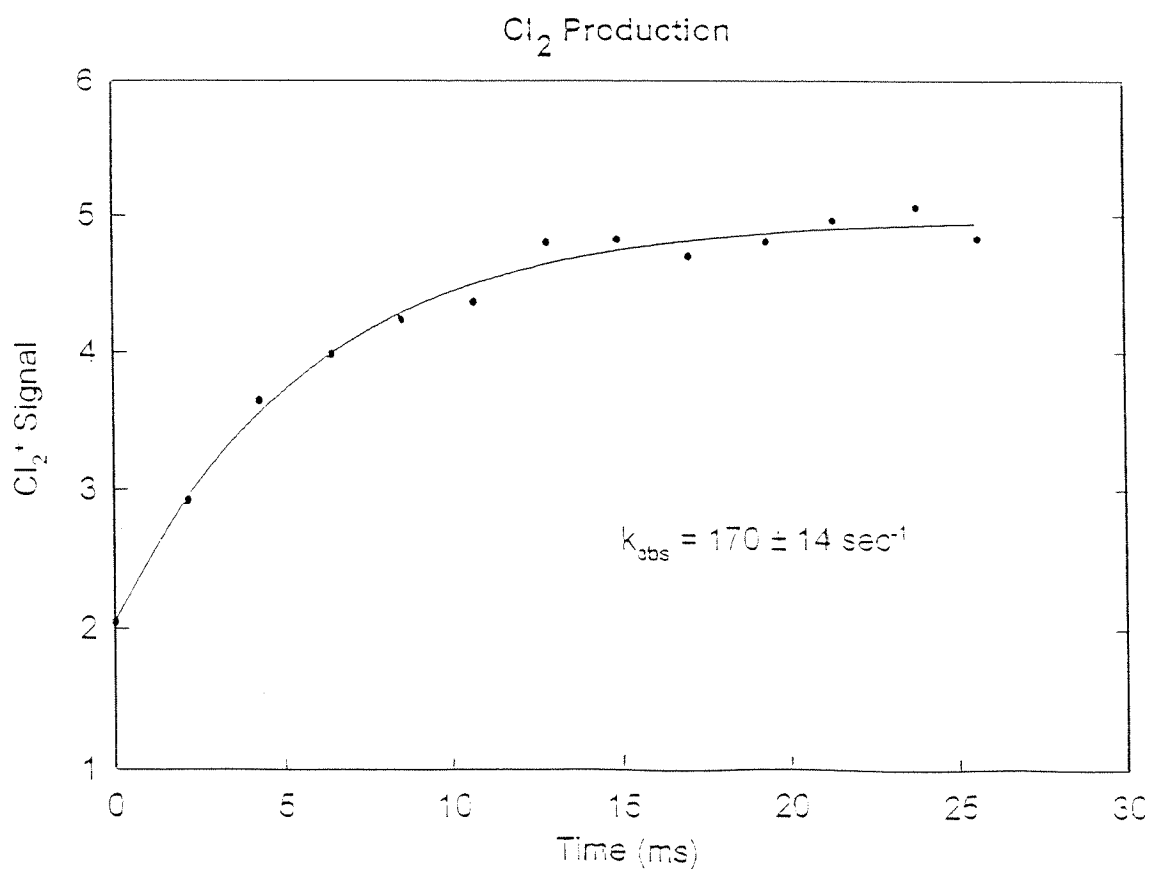
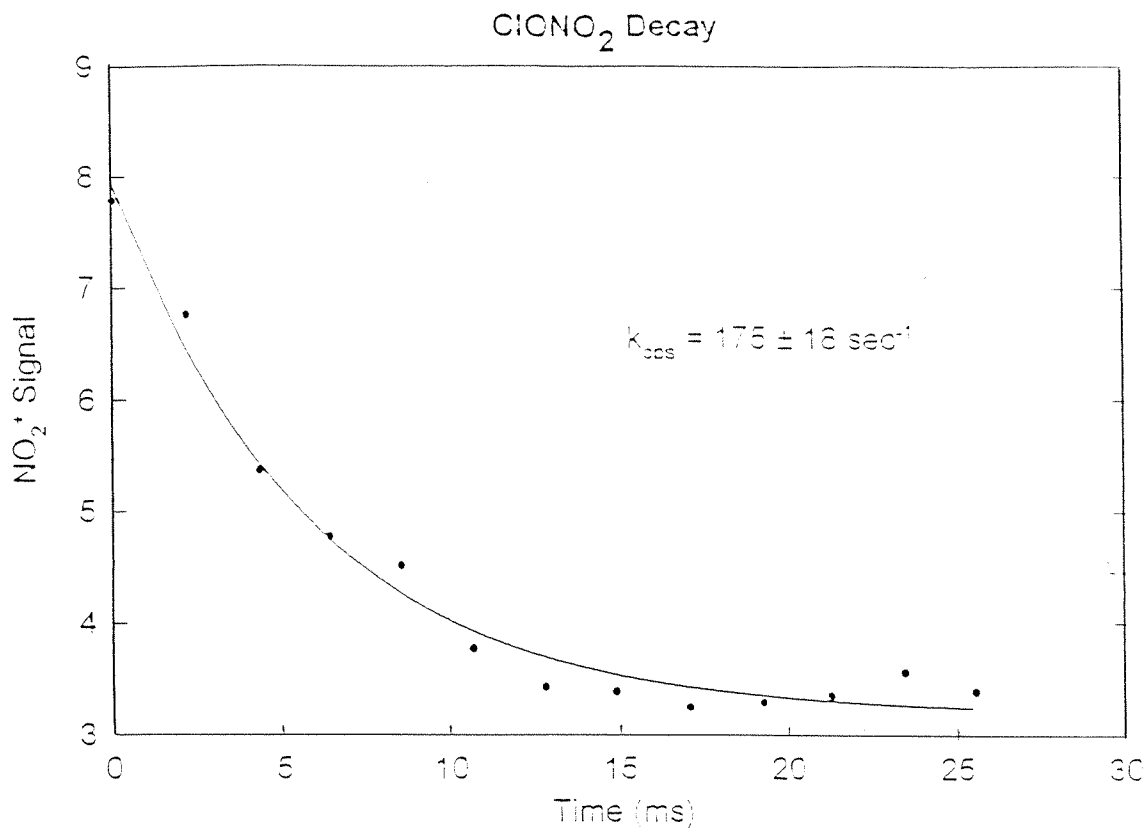


Figure 1. [ClONO₂] = 7.54x10⁻⁷ Torr, [HCl] = 7.46x10⁻³ Torr, [H₂O] = 4.81x10⁻⁴ Torr

$\text{ClONO}_2 + \text{HCl}$ on Glass Beads at -60°C

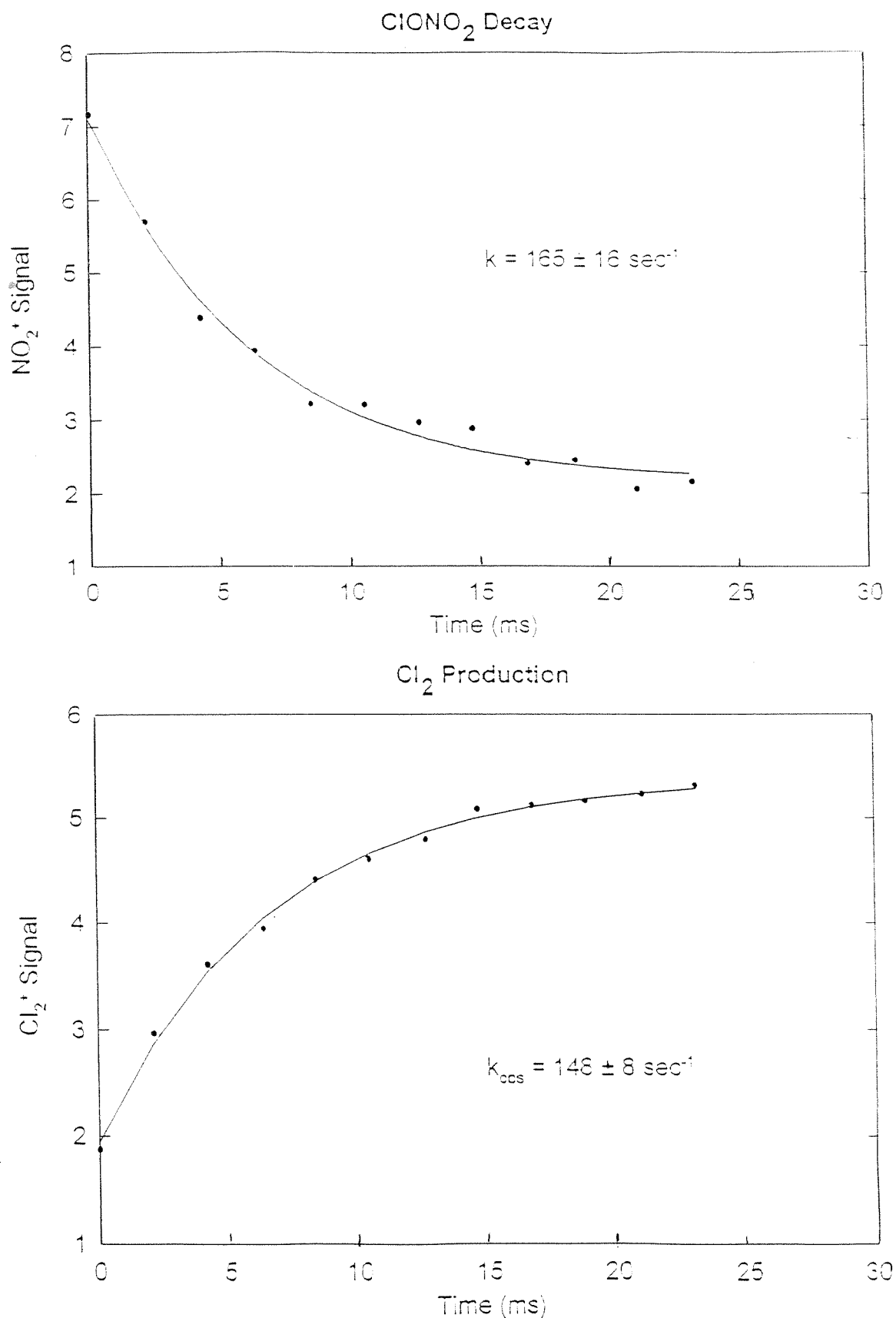


Figure 2. $[\text{ClONO}_2] = 7.81 \times 10^{-7} \text{ Torr}$, $[\text{HCl}] = 7.71 \times 10^{-8} \text{ Torr}$, $[\text{H}_2\text{O}] = 4.57 \times 10^{-4} \text{ Torr}$

$\text{ClONO}_2 + \text{HCl}$ on α -Alumina at -60°C

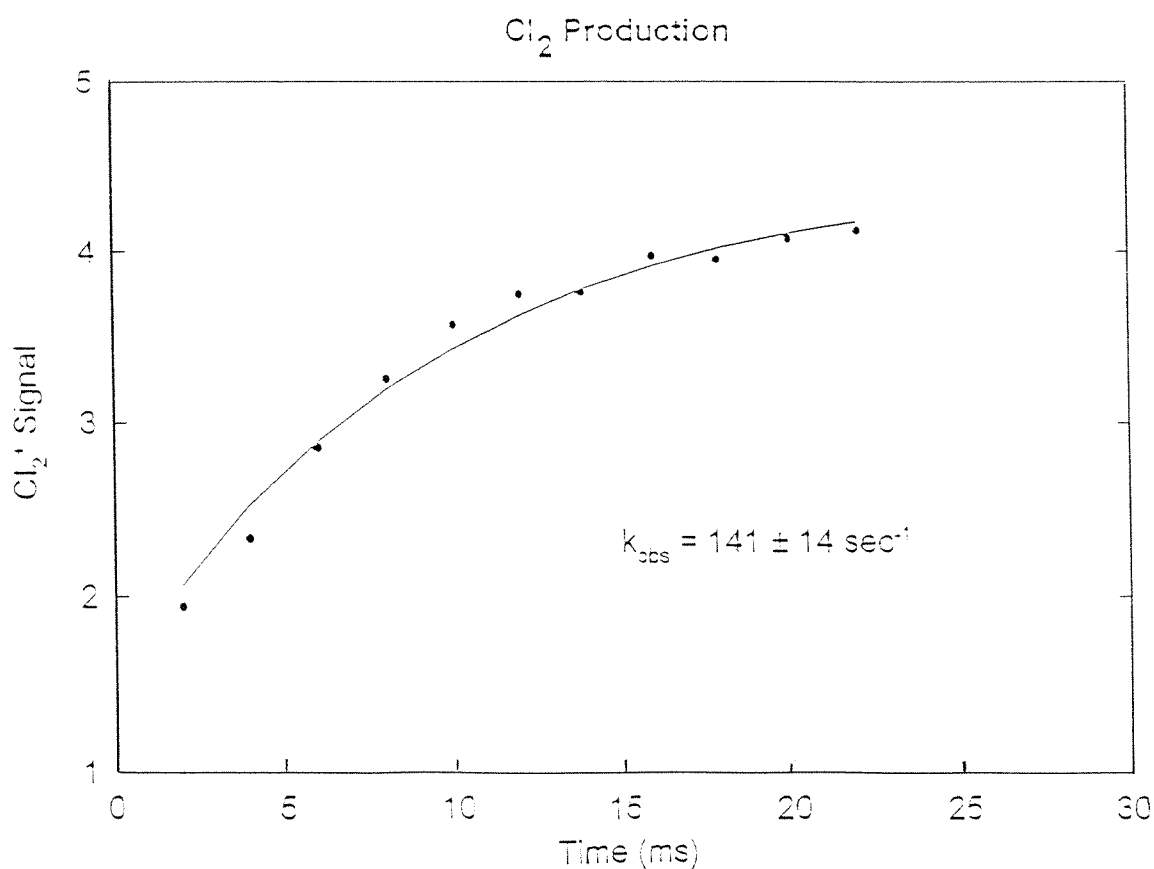
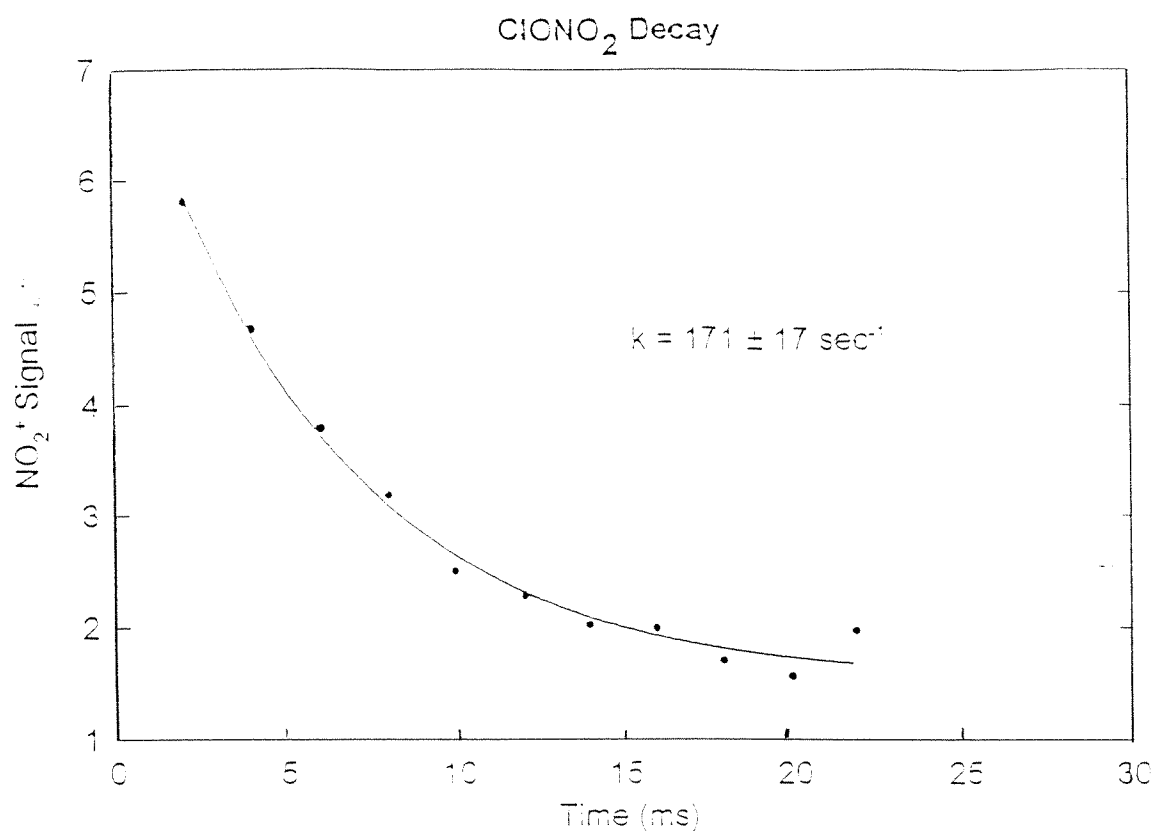


Figure 3. $[\text{ClONO}_2] = 7.56 \times 10^{-7} \text{ Torr}$, $[\text{HCl}] = 8.33 \times 10^{-6} \text{ Torr}$, $[\text{H}_2\text{O}] = 4.41 \times 10^{-4} \text{ Torr}$